Mathematical Modeling of Rechargeable Hybrid Aqueous Batteries

by

Zhixu Han

A thesis
presented to the University of Waterloo
in fulfillment of the
thesis requirement for the degree of
Master of Applied Science
in
Chemical Engineering

Waterloo, Ontario, Canada, 2014

Author's Declaration

I hereby declare that I am the sole author of this thesis. This is a true copy of the thesis, including any required final revisions, as accepted by my examiners.

I understand that my thesis may be made electronically available to the public.

Abstract

A rechargeable hybrid aqueous battery (ReHAB) system was recently developed by our research group. It has been improved via different experimental approaches, but nobody yet has tried to use mathematical modeling techniques to further understand the system. This thesis tries to investigate the ReHAB system using a few current modeling methods. The study is categorized into empirical level, electrochemical engineering level and atomistic level.

At the empirical level, a battery is simply viewed as a whole system, which means detailed descriptions in terms of the cathode, anode or electrolyte are ignored. By using the historical experimental data, researchers can predict the future behavior of a battery regardless of its internal phenomena. They usually employ some general mathematical functions, such as polynomial, logarithmic, exponential or other nonlinear functions. Currently automatic curve fitting and predicting algorithms are commonly used in the battery management system, due to the advantage in coping with the system nonlinearity. The first study in this thesis implements a tracking method called particle filter method on the ReHAB experimental data. The basic math function in the simulation is an empirical formula between the battery capacity and the Coulombic efficiency. The study confirms this correlation in the ReHABs, and proves that particle filter method can be a good option in battery performance tracking and prediction.

At the electrochemical engineering level, battery performance is simulated in the continuum models, by incorporating chemical or electrochemical reactions, transport phenomena or interfacial kinetics. This level of simulation can help observe battery electrodes in details. It is more accurate than the empirical level model, and more versatile in simulating various electrochemical problems. This thesis secondly focuses on the ReHAB system cathode and anode using finite element method, which is implemented in COMSOL Multiphysics. The study includes a design of battery system model, investigation of species distribution during cell operation, side-reaction effects and anode corrosion issues. The models designed at this level give consistent results compared with the experimental data, and illustrate some guidance for the potential experiments.

At the atomistic level, molecular simulation can model the system dynamics via step-

by-step computation. Stochastic method is an efficient molecular method to investigate electrochemical problems coupled with species diffusion and chemical reactions. Atomistic simulation commonly spends longer time, but it can be very accurate regarding the evolution of a dynamic physical system. The study at this level employs the classical stochastic method on the electrochemical deposition of Zn atoms. It is focused on the dendrite formation via implementing diffusion-limited aggregation techniques and the remaining metal ions by using stochastic simulation methods. The simulation schematically illustrates the overpotential influence on the dendrites and ion distribution at the metal surface. These findings prove that overpotential is an important factor and can also help further design of experiments.

Acknowledgements

First of all, I would like to express my greatest gratitude to my parents, without whose support I cannot happily study in Canada.

Secondly, I would like to thank my supervisor, professor Pu Chen, who has been guiding me throughout my whole master study and research.

Thirdly, I would like to send my thanks to some members in the battery group specifically. Thank you Dr. Wu, who discussed with me some electrochemical questions. Thank you Dr. Hoang, who helped my thesis and paper revision.

Fourthly, my thank goes to all the researchers in Pu Chen group, all my friends and working staffs I know in the university.

Last but not least, I would like to thank University of Waterloo to give me such an opportunity to broaden my knowledge and experience in Canada.

Dedication

This thesis is specifically dedicated to my family.

Table of Contents

List of Tables

List of Figures

Nomenclature

a	Specific interfacial area of porous electrode (m^2/m^3)
c_s	Lithium concentration of solid phase (mol/m^3)
c_l	Lithium concentration of liquid phase (mol/m^3)
$CCCV$	Constant current constant/voltage protocol
C_k	kth cycle of battery capacity (mAh)
D	Diffusion coefficient (m^2/s)
D^{eff}	Effective diffusion coefficient (m^2/s)
E^0	Standard equilibrium potential (V)
E_{corr}	Corrosion potential (V)
E_{cell}	Cell electrode potential in the simulation (V)
E_{eq}	Equilibrium potential (V)
F	Faraday's constant $(96,487C/mol)$
G	Gibbs free energy (J)
ΔG^0	Standard Gibbs free energy change (J)
ΔG	Gibbs free energy change (J)

h Stochastic simulation compartment

i_a/i_c Anodic/Cathodic current density (A/m^2)

i_{app} Applied current density in the simulation (A/m^2)

i_{ch}/i_{dch} Charge/discharge current density in the simulation (A/m^2)

i_{corr} Corrosion current density (A/m^2)

i_l Lithium current in the liquid phase (A/m^2)

i_n Local current density at the particle surface (A/m^2)

i_{side} Current density of side reaction (A/m^2)

i_0 Exchange current density (A/m^2)

I Current (A)

I_L Limiting current (A)

j Current density across electrode/electrolyte interface (A/m^2)

j_n Lithium-ion surface diffusion flux $(kg/(s \cdot m^2))$

k_{dep} Deposition event rate (s^{-1})

k_{dif} Diffusion event rate (s^{-1})

k_{dis} Dissolution event rate (s^{-1})

K Equilibrium constant

L Stochastic simulation domain (mm)

n_k Measurement noise

N_l Species flux $(kg/(s \cdot m^2))$

P_{rand} Random number in $(0, 1)$

P_{stick} Sticking coefficient

R Universal gas constant $(8.314 J/(molK))$

R_l Lithium reaction rate in the liquid phase

R_s Radius of lithium particles (m)

SOC State of charge

SHE Standard hydrogen electrode potential (V)

t Time (s)

t_+ Ion transport number of the electrolyte

T Temperature (K)

v_k State estimation noise

x_k Estimated state

z_i Species charge number

z_k Measurement data

α_a/α_c Anodic/Cathodic transfer coefficient

α_A^a Product of activities of species A in the reaction

α_B^b Product of activities of species B in the reaction

α_C^c Product of activities of species C in the reaction

β_1/β_2 Particle filter model parameters

$\gamma_{Zn^{2+}}$ Zn^{2+} activity coefficients

γ_{H^+}	H^+ activity coefficients
ϵ	Volume fraction of a phase
η	Overpotential (V)
η_{conc}	Concentration polarization (V)
η_C	Coulombic efficiency
λ	Battery degradation model parameter
μ	Chemical potential (J)
ρ	Density of film (kg/m^3)
σ	Standard deviation
σ_s/σ_l	Ion conductivity in solid/liquid (S/m)
τ	Event happening time period (s)
ϕ_s/ϕ_l	Potential of the solid/liquid phase (V)
ω	Gaussian noise

Chapter 1

Introduction

1.1 Battery History

Batteries have attracted more and more attention in recent years. They are now commonly used for energy storage in a number of electronic devices. In the mean time, electric automobile companies such as Tesla Motors are gradually changing our conventional concepts of petroleum or gas driving force into electricity driving force.

In fact, the battery has a very long history of development. It could even be derived back to the early electricity experiments in 1749 when Benjamin Franklin, the U.S. founding father interested in electricity, first used the term 'battery' to describe a set of linked capacitors with electricity [1]. At that time he created an idea that two or more objects are piled together and functioning. This idea can still explain the structure of many of today's battery cells. Afterwards the battery was developed over time when people incessantly made contributions. Guided by the basic principle of electrochemistry, different types of batteries were invented. Many people are familiar with some of the representative types listed here. In 1800 Alessandro Volta invented the voltaic cell, which was composed of zinc and copper disks. Then in 1839, the invention of fuel cell (H_2/O_2) by William Robert Grove in the UK pushed batteries to a new progress. In 1859 Gaston Plante from France invented a lead acid battery which is still widely used today. Then people created different

systems incorporating metal with metallic ions that are transferred inside the electrolyte as the internal battery current. These battery types are easily recognized nowadays, such as nickel-cadmium batteries, alkaline-manganese batteries, lithium-ion batteries, and so on. It is worthwhile mentioning that in 1991 Japanese company Sony first commercialized lithium-ion battery, and it has been popularly used in our current portable electric devices since then. However, there are still quite a number of challenging problems to deal with. Researchers in the universities, companies and other institutions are trying their best, not only to develop new types of battery systems, but to enhance the existing battery performance as well. The battery development is still prosperously going on.

1.2 Rechargeable Hybrid Aqueous Battery

The organic liquid electrolyte usually used in lithium-ion battery is not an optimal choice. The main reason is the safety issue due to its flammability and toxicity. In 1994, Dalhousie University professor Jeff Dahn first proposed the idea of the aqueous based lithium-ion battery [2]. He used $LiMn_2O_4$ and VO_2 as electrodes and 5M $LiNO_3$ in water as the electrolyte. It provided a nice solution to the traditional lithium-ion battery problem. From then on, more aqueous battery types followed the milestone made by Dahn [3–6].

A new type of rechargeable hybrid aqueous lithium-ion battery (ReHAB) was invented by professor Pu Chen's research group in 2012 [7]. This type of battery uses lithium intercalation compounds $LiMn_2O_4$ as the cathode material, metal Zn as the anode material, and acidic Zn^{2+} and Li^+ ions water based solution as the electrolyte. This combination significantly alleviates the safety problems from the non-aqueous typed battery; additionally it has an important advantage of low cost.

At the cathode side, lithium ion is intercalated into $LiMn_2O_4$ during the discharge process or de-intercalated from $LiMn_2O_4$ during the charge process. It is usually expressed as follows [8].

$$LiMn_2O_4 \leftrightarrows Li_{1-x}Mn_2O_4 + xLi^+ + xe^- \tag{1.1}$$

When a battery is charged, the cathode is oxidized, meaning Li^+ is extracted from the $LiMn_2O_4$ tetrahedral sites. In contrast, when a battery is discharged, the cathode is

reduced, meaning Li^+ is inserted into the $LiMn_2O_4$ tetrahedral sites. Researchers have found that two steps usually occur during Li^+ intercalation and deintercalation. During cyclic voltammetry (CV) testing, it has been observed that in the charging process, Li ions from half of the tetrahedral sites with Li-Li interaction are extracted at around 4.05V (versus Li/Li^+ equilibrium potential), giving an obvious peak. Then the second peak at 4.15V (versus Li/Li^+ equilibrium potential) illustrates another extraction of Li ions from the other half of the tetrahedral sites without Li-Li interaction [9].

At the anode side, Zn^{2+} is deposited on the Zn surface during the charge process or dissolved back to the solution during the discharge process. Written in the simple chemical reaction formula, these processes are just Zn electrochemical reactions.

$$Zn \leftrightarrows Zn^{2+} + 2\,e^- \tag{1.2}$$

Comparison with cathode makes it clear that when the battery is being charged, the anode is reduced, thus Zn^{2+} ions are deposited on the Zn anode side. Conversely, Zn is oxidized to Zn^{2+} during the discharge process.

In this case, the anode and cathode appear to be undergoing their own ion transfer processes during charge and discharge, when the electrolyte acts as an ion reservoir providing Li^+ and Zn^{2+} sources for the electrochemical reactions. This whole process is illustrated schematically in the Figure 1.1 [7].

However, in a battery system, the amount of electrons generated/consumed in the cathode by Li^+ ion transfer should be strictly equal to the amount of electrons consumed/generated in the anode by Zn^{2+} ion transfer. This is how the anode and cathode are linked together in the ReHAB, the principle of which is quite different from the conventional rocking-chair lithium-ion battery [10](Lithium-ion is intercalated into one electrode, and at the same time, lithium-ion is deintercalated from another electrode. The flow of electrons is only driven by the flow of lithium-ions). Thus, ideally the electron activity should only be related to the Zn deposition/dissolution and lithium-ion intercalation/deintercalation. But in fact, as with other battery systems, related issues can seriously influence ReHAB's performance. The most harmful problems happening inside the battery during charge and discharge are extra chemical reactions and self-discharge issues. Because of the aqueous

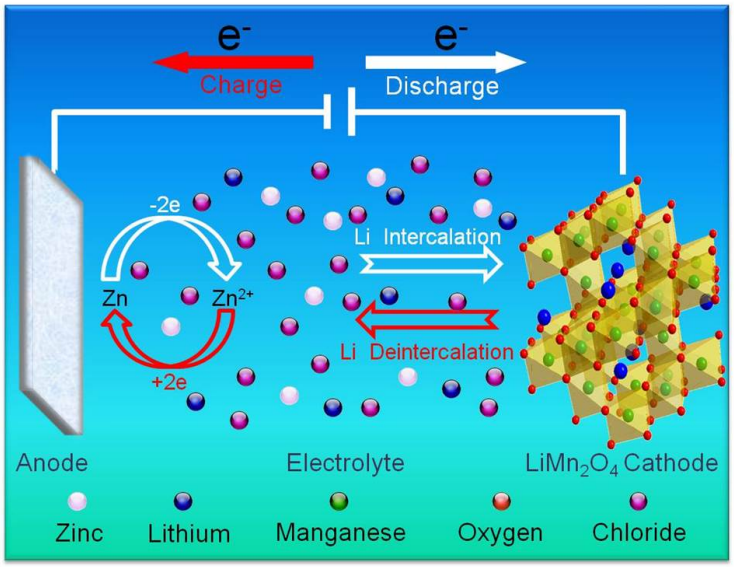

Figure 1.1: ReHAB Schematic Image

solution environment, the potential window has to be restricted within the equilibrium potential of H_2 evolution and O_2 evolution. It is worth noting that in the aqueous electrolyte solution, the electrochemical stability should be limited to around 1.2V [11]. There are many forms of reactions possibly generating gas, for example,

$$2\,H_2O \longrightarrow O_2(g) + 4\,H^+ + 4\,e^- \tag{1.3}$$

$$4\,OH^- \longrightarrow O_2(g) + 2\,H_2O + 4\,e^- \tag{1.4}$$

$$2\,H^+ + 2\,e^- \longrightarrow H_2(g) \tag{1.5}$$

$$2\,H_2O + 2\,e^- \longrightarrow H_2(g) + 2\,OH^- \tag{1.6}$$

It is still unclear whether one or several reactions happen in the ReHAB, but since ReHAB has acidic electrolytes and a Zn anode, one unwanted chemical reaction could be definitely happening at the anode.

$$Zn + 2\,H^+ \longrightarrow Zn^{2+} + H_2(g) \tag{1.7}$$

This reaction at the anode causes Zn corrosion, which seriously consumes electrode

material Zn and change the electrolyte environment pH. In the lab, researchers search for protective materials to restrain the influence; in this thesis study, a model is intended to explain the fundamental mechanism, reproduce the experimental results by simulation, and guide the future experiments.

At the cathode side, $LiMn_2O_4$ material has been known to be thermodynamically unstable for years. At the end of discharge when Mn^{3+} is at high concentration, a disproportionation reaction may happen [12].

$$2\,Mn^{3+}(s) \longrightarrow Mn^{4+}(s) + Mn^{2+}(l) \tag{1.8}$$

This reaction can cause Mn^{2+} to be generated and dissolved into the aqueous electrolyte, and is identified by researchers as an important reason for battery capacity fading.

1.3 Battery System Modeling

As mentioned above, different levels are associated with relevent methods in the current research on battery modeling. Researchers have developed a number of standardized approaches to the design and realization of their goals. Obviously there is not an absolutely accurate model which produces the same results as the experiments. Model design is usually incorporated with idealization, parameter tradeoffs and error trial methods. Via iterative refinements, models can give inspiring discoveries out of the experimental data. Nowadays, modeling has gradually become a very popular research methodology.

1.3.1 Empirical Model

It might be conceived that a mathematical model is simply created out of abstract concepts, for example, the famous Newton's Law describes natural physics in the mathematical forms such as acceleration and forces. But more often researchers are confronted with batches of experimental data with no idea of any physics or chemistry concealed beneath. Therefore at the starting stage, theoretical model is usually based on some initial assumptions. Unsatisfied may these assumptions in the model implementation process initially, they should

be adjusted in a correct cycle. One model approach is to combine the experimental data with the model design, and the real data can indeed help theoretical achievement. This is called empirical model.

The general philosophy of designing an empirical model does not vary a lot even though there are widespread applications. It is named empirical because it highly relies on data. With enough experimental data collected, modelers try to find out how to make an optimal combination of the known parameters and real conditions that can provide accurate descriptions [13].

Many techniques can be used for empirical modeling. One of the commonly used methods is the regression curve (Linear, Quadratic, Exponential, etc.). However, since battery is a chemical system, it cannot simply obey the laws of strict functions. Even at the system level faced with simple cell performance (for example battery capacity and battery voltage), one needs to come up with a method to cope with the existing nonlinearity in the experimental data. Recent years have seen a dynamic development of modeling techniques. They have been gradually used in the battery management system. These modeling algorithms can precisely track and predict battery performance. The initial design of these models usually considers factors such as internal resistance, charge/discharge type or charge/discharge rate [14], and the execution focuses more on how to mathematically fit the modeling data with the experimental data.

1.3.2 Electrochemical Engineering Model

In terms of insight studies of materials, physics and chemistry can be explained using continuum modeling strategies. This level is described as electrochemical engineering modeling. When one wants to model an object as a continuum, it is assumed that the substance of the object completely fills the space it occupies [15]. The fact that the matter is made of atoms is ignored; even though on length scales greater than atomic distance, a satisfactory accuracy can still be obtained. Continuum models usually deal with problems in solids or fluids. Under some general physics governing principles such as conservation of mass, conservation of momentum and conservation of energy, different parameters and unknown variables are bundled together into a set of partial differential equations.

There are various modern techniques in solving these complicated equations. Since it is almost impossible to solve these equations analytically, people have derived the standardized numerical methods. Confronted with partial differential equations, researchers sometimes use finite volume or finite difference methods. These methods can successfully change the continual mathematics into discrete forms, but when the system equations become intertwined with each other, finite element method is usually chosen. Finite element method is a step-by-step computational method. The whole process of finite element analysis is generally divided into the following stages: discretization, derivation of equations, assembly, and postprocessing [16].

Finite element method emphasizes that a continuous function can be approximated using discrete models by discretization. A complex region defining a continuum can thus be discretised into several simple shapes. Each shape, named an element, has several points called nodes. Each element's behavior is expressed using some interpolation functions (for example polynomial functions) with respect to its individual nodal behavior. Elements' behavior, which is a physical property (for example mechanical forces, heat flow, or in the case of batteries' electric current) can be related to the nodal behavior, which is another physical property (for example displacement, heat velocity, and lithium-ion concentration). This relationship is derived exactly from the partial differential equations.

Lithium-ion battery model at the continuum level is very complicated. It can be simplified with a total of five governing equations, five dependent variables and two independent variables at most [17]. If more conditions are added inside, solving the problem would be very difficult. COMSOL Multiphysics is a powerful tool to cope with such complex partial differential equation problems [18]. It has some specific libraries such as Electrodeposition Module and Battery & Fuel Cells Module designed for battery modeling [19].

1.3.3 Atomistic Model

Molecular dynamics has been frequently used in a system whose behavior can be simulated in time dependent molecular interactions. Equations derived from the fundamental physics and chemistry are coupled together. The complexity of computations largely depends on

the parameters involved in the equations and the number of considered conditions. The extreme case can cause very long processing time.

However when the calculation of the molecular interaction potentials and forces becomes quite handy, people try to resort to other global optimization techniques [20]. Thermodynamics equilibrium properties are static averages independent from the process of dynamics of the system. One widely used technique is called Monte Carlo (MC) method [21]. The essence of the Monte Carlo algorithm is a heuristic description of a plausible pattern of changes which are in the configuration assumed by the whole system [22]. From the standard Metropolis Monte Carlo algorithm for example, an acceptance of a trial step of move relies on the potential associated with this tempted move. This acceptance ratio is expressed by a probability,

$$P_{r_{old} \to r_{new}} \propto exp[-\frac{U(r_{new}) - U(r_{old})}{k_B T}] \tag{1.9}$$

in which k_B is the Boltzmann constant. The characteristic of the stochastic method is its utilization of random numbers. Every calculated probability is postprocessed by a comparison with a random number. The comparison is the criterion to decide whether to move or not.

Kinetic Monte Carlo (KMC) method, which is a branch from the Monte Carlo statistical simulation family, has provided a pretty simple, yet powerful and flexible approach to stochastically simulate systems having many processes and behaviors, such as chemical reactions or species diffusion [23]. It is right now commonly used in the chemical and biological systems. Well-conditioned atomistic simulations have shown highly consistent results with the experiments.

1.4 Objectives

All the studies in this thesis are examined around the ReHAB, covering empirical level, electrochemical engineering level and atomistic level. The overall objectives of this thesis can be summed as follows:

1. Track and predict ReHAB cell capacity via a principle proposed in the literature;
2. Develop a continuum model for ReHAB system and test battery cycles in simulation;
3. Study the anode system with corrosion issues, and compare modeling results with the experimental data;
4. Study the dendrite formation and remaining ion distribution during electrodeposition correlated with overpotential.

In order to achieve the goal, detailed theory and methodologies used in this thesis are:

1. Particle Filter method on the assumption of capacity degradation model;
2. Lithium-ion battery interface with Butler-Volmer theory, ion transport theory, porous electrode theory and Nernst-Planck interface;
3. Metal corrosion on the Nernst-Planck interface;
4. Diffusion-limited aggregation techniques and stochastic simulation algorithms.

1.5 Structure of Thesis

The thesis is organized into six chapters.

- Chapter 1 gives a basic introduction of battery history, ReHAB system structure and common modeling methods.
- Chapter 2 reviews the related literature, illustrating the general ideas of models at different levels.
- Chapter 3 focuses on the empirical level. The background knowledge of particle filter technique is presented at first. Then this technique is implemented on the experimental data. An assumption correlating Coulombic efficiency and battery capacity is incorporated for cycle tracking and prediction.

- Chapter 4 focuses on the electrochemical engineering level. In the first cathode-focused section, background knowledge of pseudo 2D porous electrode theory is given at the beginning. Butler-Volmer kinetic and anode Tafel kinetic connect $LiMn_2O_4$ and Zn together. The model simulate battery charge/discharge curve, ion distribution during discharge and capacity fading during constant-current constant-voltage tests. Modeling results are compared with experimental results. In the second part, corrosion theory is firstly introduced. The model focuses on the Zn corrosion in the thermodynamics simulation. The simulating results address Tafel curve with pH values, and compare them with the experimental results.

- In Chapter 5, the general theory on stochastic method is presented. The electrodeposition simulation in the study is restricted in the diffusion-controlled region. In the first part, the simulations are implemented on the dendrite formation with different sticking coefficients. In the second part, remaining metal ion distribution is simulated via the stochastic method. All the stochastic simulations in this chapter can clearly illustrate the overpotential influence.

- Chapter 6 concludes what has been done and discusses the potential future work.

Chapter 2

Literature Review

The previous chapter has generally introduced the basic knowledge of batteries and modeling methods. This chapter will include more detailed research accomplishments. Three levels of modeling are separated into three sections.

2.1 System Model Design

Modeling at the system level is similar to the situation when a driver wants to know how far he can drive his car until he has to refuel the tank, but only from the information he obtains from the meter. He can make predictions for the decrease of the oil in the tank on the basis of historical data. He can estimate the health of his car. He can also propose solutions if his car does not stay at the standard of health conditions. System simulations on the battery performance think in a similar way. Researchers design methods and algorithms in order to predict and track the voltage or capacity performance, evaluate batteries' state of health (SOH), and give suggestions to the optimization of materials.

Remaining useful performance (RUP) is widely acknowledged as one of the important metrics to evaluate batteries from the view on the system level [24]. It is defined as the time length from starting to make observation to the end of performance (EOP) criterion is reached. EOP is another terminology in the battery research and application. It is

the time period when the maximum available capacity (or sometimes used as voltage) is reduced to a particular threshold, for an instance, 80% of its initial value [25] [26].

There are various factors influencing the RUP evaluation. It might be unexpected noise, for example environmental noise or operational noise, and researchers design algorithms to cope with the uncertainties [27]. It might be the difficulties from evaluating the maximum capacity [28]. But the most critical issue is the unclearness of how to incorporate the batteries internal characteristics, such as internal impedance [29], the normal battery testing measurement, such as cycles testing [30], and other side effects, such as side reactions [31].

There are generally two approaches to the system modeling, physics-based and data-driven. As mentioned above, electrochemical impedance spectroscopy (EIS) measurement can help establish a robust battery model [32], but the high accuracy requirements and complexity often make the procedure hardly manageable. On the other hand, simple models based on the raw data cannot reveal a deeper interpretation of the battery materials. Thus experimentalists and modelers cannot establish a mutual communication on the battery system. A common way people choose to model on the system level is to design the model parameters based on the physics assumptions, and fit the model results based on the experimental data, for example the neural network model [33] or circuit filtering model [34]. Via this approach, model design links background physics and system data together.

2.2 Electrochemical Engineering Model Description

In 1959 physicist Eugene Wigner delivered an astounding lecture titled "The Unreasonable Effectiveness of Mathematics in the Natural Sciences". In his speech, he addressed that the mathematical formulation can lead in an uncanny number of cases to an amazing description of a large class of phenomena [35]. As a self operational system, battery has attracted scientists to try to use complicated but well organized groups of partial differential equations to explain phenomena, predict future performance, and help design better cells.

A general model for lithium-ion batteries was firstly developed by Doyle and Newman from University of California, Berkeley [36]. Since then researchers developed numer-

ous pseudo 2D battery models to study different battery phenomena. Professor Ralph E. White at the University of South Carolina has contributed a series of first principle lithium-ion battery models. Some models neglect transport of lithium in electrolyte phase under charge/discharge current [37]. Some models are developed to simulate the loss of active materials due to electrochemical solvent reduction reaction at the anode/electrolyte interface [38]. Various cathode and anode materials are selected in the theoretical models. To solve the real battery issues, many models also have incorporated detailed descriptions such as materials internal structure, Solid Electrolyte Interphase (SEI) formations, etc.

The battery system is only one kind of electrochemical system, but there are a lot more models on other systems. In the corrosion area, various models on the issues such as corrosion processes or material influence are developed. For example, Sharland designed a model focusing on the propagation stage of an established pit during the corrosion [39]. Walton's work on the crevices and pits in iron studied species transport during corrosion [40].

Among numerous models at this level, finite element method is one of the most widely used techniques. It can help solve the problems like ion flows or exchange currents [41]. Meanwhile it also helps battery design with multiphysics problems such as heat runaway [42], geometrical thickness [43] or loading tests [44].

2.3 Atomistic Model Computation

Electrodeposition process is an important technology for the fabrication of electric devices [45]. Accompanied with experimental studies, computational methods provide a more sophisticated view [46]. In the last section discussion, continuum computation methods on a set of partial differential equations are implemented on the condition that the characteristic length is greater than the molecular scale [47]. However, in terms of nano scale, atomic simulation has the priority.

Kinetic Monte Carlo (KMC) is a widely used stochastic method in the atomistic simulation [48]. The advantage of KMC is that it can perfectly simulate a evolving system

dynamically from one state to another state [49]. Meanwhile in the electrodeposition application, many processes such as surface adsorption, dissolution, diffusion and reactions happen simultaneously [50–52]; thus this static method has been used more and more frequently.

In the recent years, more work has been contributed to the approaches to speed up KMC algorithm in multiscale approaches, including methods like coarse-grained [53] KMC method and spatially adaptive coarse-grained KMC method [54] [55]. People are mainly trying to find a better algorithm, because in the diffusion-adsorption-reaction system, diffusion rate is weigh larger than the other rates, which takes too long time to make the system evolve (meaning deposition height getting thicker) [56]. Apart from this effort, some groups also try to combine partial differential equations (PDE) with stochastic methods [57], which is considered to be accurate and highly efficient right now.

Chapter 3

Empirical Models

3.1 Introduction

Battery system level models have been studied frequently in the recent years. Most of the parameters in the applications are related to the battery conditions such as cycle numbers, battery capacity, battery state-of-charge (SoC), etc [58]. The ultimate goal of these studies is mostly to better control the battery system [59]. For example, some papers focus on the study of remaining useful level (RUL), in which case they can understand when battery will no longer maintain useful [60].

But few studies have tried to bridge the gap between the system level study with material level study. One important reason is because most system models are trying to develop more robust methods, and apply the methods on the raw battery data. While on the other hand, there is a strong need to understand a system with a specific material or charging protocol via system level modeling.

A rechargeable hybrid aqueous battery (ReHAB) system was recently developed by professor Pu Chen's research group [7]. Researchers have tried different methods to further investigate either the material properties or the best optional materials for the system. This chapter aims to apply a standardized particle filter model on different materials in the system. Via the empirical model and the intrinsic model establishment principles, the

study further reveals the selected material properties.

3.2 Experimental Section

Electrolyte preparation: 110.28g of Li_2SO_4 (Alfa Aesar, 97%) and 146.71g of $ZnSO_4$ $7\,H_2O$ (Alfa Aesar, 98%) were added into 250mL of deionized water under vigorous stirring. The stirring was continued overnight and the volume of the obtained solution was adjusted to 500 mL. pH of the electrolyte was adjusted to 4.00 ± 0.05 by a few drops of 1M H_2SO_4 solution.

Anode preparation: commercial zinc foil (Alfa Aesar) was polished using $0.3\mu m$ zinc powder (Boehler) dispersed in de-ionized water and a mesh (Boehler). Droplets of the zinc powder suspension were added onto zinc surface while the mesh was manually crushed back and forth on the surface for 10 minutes. Polished zinc foil was washed with soap and deionized water, followed by rinsing with ethanol and dried at 60^oC under vacuum for 30 minutes. Zinc anode was prepared from polished zinc foil by mean of electrode cutter.

Cathode preparation: 1.72g of $LiMn_2O_4$ (MTI) was mixed with 0.14g of carbon KS-15 or SFG-6 (Timcal). The obtained mixture was added in 2.80g solution of polyvinylidene fluoride (5%) in N-methy1-2-pyrrolidone (Sigma Aldrich). The system was mixed in an automatic mixer for 2 minutes; the mixture was casted onto a polyethylene (PE - All-spec) paper. The casted cathode on PE was heated under vacuum at 60^oC for 1 hour before cut by mean of electrode cutter.

Battery assembling and testing: cathodes were immersed in electrolyte in vacuum for 20 minutes before battery assembling. Celgar separator was wetted with several drops of electrolyte and placed in between anode and cathode. Both Swagelok cells and coin-cells were used. The batteries were cycled on a Neware battery tester (Neware Co. Ltd.). Each cycle consists of a rest period of 1 minute, constant current charge at 1C rate, and rest for 1 minute, followed by constant current discharge at 1C rate.

3.2.1 Experimental Results

Batteries assembled with two different carbon conductors and two different cells are studied in the lab. Two carbon sources are KS-15 and SFG-6. Both coin cells and Swagelok cells were used. Each system was tested three times to ensure repeatability, which sum up to twelve samples altogether. The batteries were charged/discharged at 1C rate. The tests were run at room temperature (25 ± 2^oC). The charge/discharge capacity was recorded in each cycle. In this chapter, only discharge capacity of different batches is used in the further simulation. The following tables from 3.1 to 3.4 illustrate the results obtained from the experiments. Each table shows three repeated cells' capacities at 20th, 320th and 800th cycles. The values listed in the columns μ and σ represent average values of three batches of samples and their standard deviations. From the tested data, we can find coin cells preserve better performance compared with swagelok cells, since most coin cells' 800th capacities are around 0.2 mAh while swagelok cells' capacities are around 0.13 mAh or even lower. This is due to the fact that coin cells are assembled in the glove box with vacuum circumstances, but the swagelok cells are assembled directly in the open air. Thus the latter ones are more likely to be affected by environmental factors such as oxygens and humidity.

Table 3.1: Coin Cell/KS-15 Data

Cells	20^{th}[mAh]	320^{th}[mAh]	800^{th}[mAh]
1	0.458	0.282	0.184
2	0.472	0.304	0.201
3	0.469	0.272	0.188
μ	0.4663	0.2860	0.1910
σ	0.0074	0.0164	0.0089

The simulation uses data from cycle 20 to cycle 800. The reason for this selection is because lithium ion battery's first cycle and second cycle capacity are mostly different. This capacity difference will maintain when the calculation model ($C_{k+1} = \eta_{C,k}C_k$) is implemented. However this is not due to the non-linearity term between calculation and measurement, which will be further discussed in the model section. In order to avoid this

Table 3.2: Coin Cell/SFG-6 Data

Cells	20^{th}[mAh]	320^{th}[mAh]	800^{th}[mAh]
1	0.446	0.292	0.188
2	0.475	0.320	0.225
3	0.473	0.332	0.240
μ	0.4647	0.3147	0.2177
σ	0.0162	0.0205	0.0268

Table 3.3: Swagelok Cell/KS-15 Data

Cells	20^{th}[mAh]	320^{th}[mAh]	800^{th}[mAh]
1	0.535	0.350	0.132
2	0.473	0.282	0.128
3	0.479	0.316	0.140
μ	0.4957	0.3160	0.1333
σ	0.0342	0.0340	0.0061

Table 3.4: Swagelok Cell/SFG-6 Data

Cells	20^{th}[mAh]	320^{th}[mAh]	800^{th}[mAh]
1	0.509	0.344	0.170
2	0.515	0.230	0.056
3	0.529	0.349	0.155
μ	0.5177	0.3077	0.1270
σ	0.0103	0.0673	0.0576

influence on the model, cycle 20 is chosen to be the starting point for comparison and implementation.

3.3 Model Implementation

3.3.1 Model Definition

Empirically, the battery is simply viewed as a whole system, which means detailed descriptions in terms of the cathode, anode or electrolyte are ignored. General mathematical functions such as polynomial, logarithmic, exponential or other nonlinear functions are commonly utilized. Accessing these functions is not totally from scratch, but actually it is developed by interpreting a battery system.

One approach to understand a battery system is by using a circuit model. The losses in a battery such as the voltage drop due to its internal impedance (which is IR drop), concentration or activation polarization can be described by a standard lumped parameter model [61]. As show in the Figure 3.1, the battery system is composed of a resistor R_E and an RC network connected in series. The resistor R_E describes the electrolyte resistance, or other resistance generated by the charge accumulation and dissipation. The RC network illustrates the charge transfer effects, when the R_{CT} is understood as the charge transfer resistance, R_W is known as concentration polarization effect encapsulated as Warburg impedance and C_{DL} is explained as diffusion capacitance. Simple as the lumped parameter model seems to be, the usual electrochemical analysis such as lithium-ion battery charge/discharge curves and frequency domain graphs are derived from this model.

An empirical model proposed frequently to simply describe the battery capacity degradation is given as follows [62].

$$\lambda = a \exp(-bt) \tag{3.1}$$

where a and b are model parameters, t is the time of cycles and λ is the internal battery performance related parameter such as R_{CT} or R_E in the lumped parameter model. In the real battery testing, battery performance is usually under the metrics of capacity. In this case, C/1 capacity can be considered here as λ, and it can be observed that the capacity is degrading based on the model.

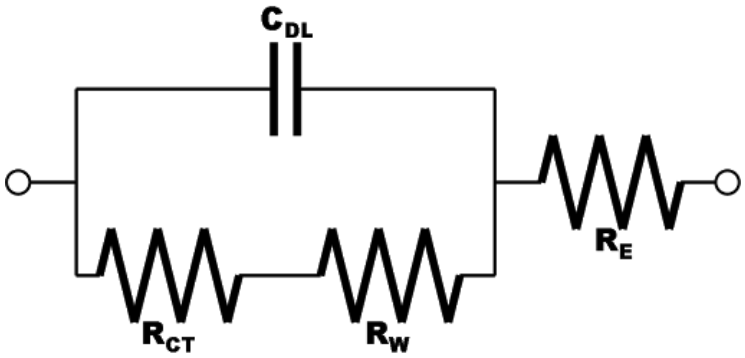

Figure 3.1: Lumped Parameter Model

According to the model presented, it can be rewritten in a new form:

$$C_k = \exp(-b_k \Delta t) C_{k-1} \tag{3.2}$$

where $t_k = t_{k-1} + \Delta t$. The reason parameter b is expressed with respect to k is because it is very likely that the degradation rate is different at different cycle. However the problem for this model is that b_k cannot explicitly reflect the properties or measurements of real batteries. At the same time, it is also too tedious to calculate b_k at every cycle. In order to understand how the parameter b_k is related to the battery observation, there is a further model proposed:

$$C_{k+1} = \eta_C C_k + \beta_1 \exp(-\beta_2 / \Delta t) \tag{3.3}$$

In this expression, Columbic efficiency and capacity are correlated at each cycle. The second term on the right being accounted is a description of the self-charge factor during test, in which Δt is the time duration for each cycle interval and β_1,β_2 are parameters to be determined. Different battery cells have different values of the second nonlinear terms. The values depend on the certain battery material properties, battery running environment conditions or how well the battery can resume the capacity during the resting time. To simplify the model equation, it is written as

$$C_{k+1} = \eta_C C_k + M \tag{3.4}$$

where M denotes a nonlinear term.

Based on the definition of Coulombic efficiency, it is expressed as follows [63].

$$\mathrm{CE} = \frac{Q_d}{Q_c} = \frac{\text{Charge out}}{\text{Charge in}} \tag{3.5}$$

As defined above, CE is a ratio between one charge and discharge, which illustrates the energy removed from a battery during discharge compared with the energy used during charging to restore the original capacity. It reflects the charge efficiency or charge acceptance of a battery. But from the system level model, Coulombic efficiency becomes a connection between two consecutive cycles. In this paper, this empirical model is implemented via particle filter method.

3.3.2 Particle Filter Method

Particle filtering method is a Monte Carlo sampling method for inferring a specified performance in the state-space models. The state of a system evolves over time. Meanwhile we also measure the system state at each step. The measurement has noise combined, which is why we need filtering method [64]. Expressed by a standard mathematical formula, the state of the system evolves as:

$$x_k = f_k(x_{k-1}, v_{k-1}) \tag{3.6}$$

where x_k represents the state of the system at time k, v_k is the state noise vector, and f_k is a possible non-linear and time-dependent function describing the evolution of the state vector. The state information x_k is unobservable, or in another word hidden, while the information about x_k can be obtained through the measurement of its z_k, which is expressed as:

$$z_k = h_k(x_k, n_k) \tag{3.7}$$

where h_k is another non-linear and time-dependent function describing the measurement at every step, and n_k is the measurement noise.

There are two steps in the filtering process, prediction step and update step. We denote all the measurements up to the time k as $z_{1:k}$. In this case, in the Bayesian setting, the problem can be formalized as finding the distribution $p(x_k|z_{1:k})$, which is also named probability density function (PDF). In the prediction step, we only have the information

of PDF up to $k-1$, which is $p(x_{k-1}|z_{1:k-1})$, and we want to have the prediction for the next step state $p(x_k|z_{1:k-1})$. The math function is

$$p(x_k|z_{1:k-1}) = \int p(x_k|x_{k-1})p(x_{k-1}|z_{1:k-1})dx_{k-1} \tag{3.8}$$

$p(x_{k-1}|z_{1:k-1})$ is the previous particle filter calculation result, which can be recursively used. $p(x_k|x_{k-1})$ can be obtained by our defined function $x_k = f_k(x_{k-1}, v_{k-1})$.

Here the knowledge of $p(x_k|z_{1:k-1})$ can be understood as prior knowledge of x_k, but it needs to be updated when we receive the measurement of z_k. Thus naturally in the update step, based on the Bayesian rules, there is a formula:

$$p(x_k|z_{1:k}) \propto p(z_k|x_k)p(x_k|z_{1:k-1}) \tag{3.9}$$

in which $p(z_k|x_k)$ can be calculated from $z_k = h_k(x_k, n_k)$ and $p(x_k|z_{1:k-1})$ is introduced before.

During the update step, there is an added procedure called importance sampling which is a Monte Carlo procedure. In this procedure, we need to calculate the likelihood of all the particles compared with the measurement. The reason is that some particles might not correctly reflect the true measurement, and we need to discard these particles; and some particles are just correctly reflecting the true measurement, and we need to keep these particles and even duplicate these particles for several times. The expression of the likelihood function is expressed as

$$L(z_k|x_k^i, \beta_k^i, \sigma_k^i) = \frac{1}{\sqrt{2\pi}\sigma_k^i} \exp[-\frac{1}{2}(\frac{z_k - x_k^i(\beta_k^i)}{\sigma_k^i})^2], \qquad i = 1, \ldots, n \tag{3.10}$$

where i defines the ith particle. Each particle thus is given a weight by normalization. Compared with a random number generated, it can be decided whether to be eliminated or duplicated. The two-step prediction and update processes can be illustrated in the Figure 3.2.

After first tens of cycles of prediction and update processes, the estimated parameters for our current tested battery are obtained. Based on Jeff Dahn's Coulombic efficiency series of publications [63, 65–69], Coulombic efficiency will gradually stabilize when cycle

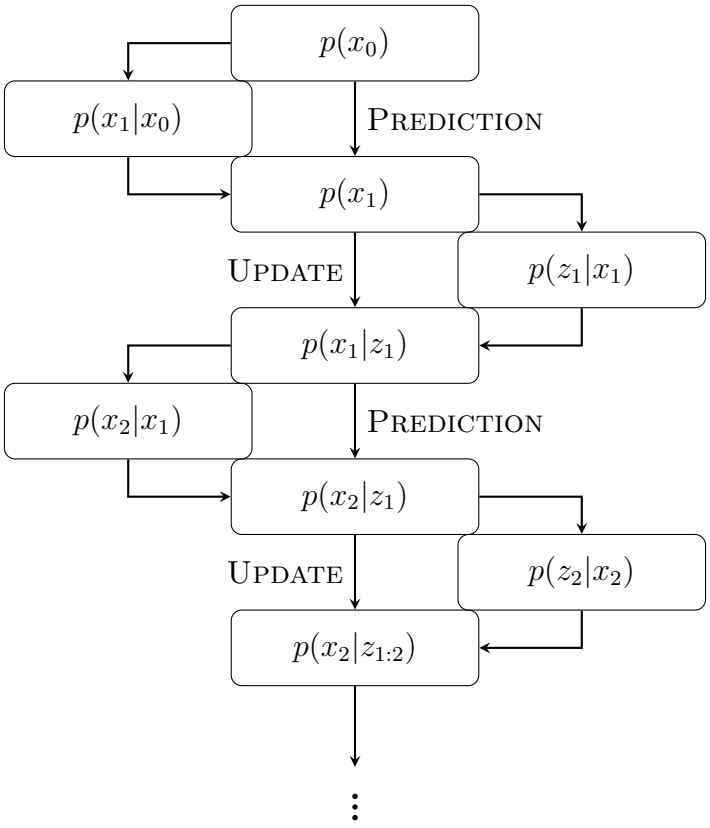

Figure 3.2: Flow Chart of PF

number increases. A stabilized Coulombic efficiency is assumed and used for future cycle predictions.

In the battery measurement and processing operations, measurement noise n_k and state estimation noise v_k are both added as Gaussian noise $\omega \sim N(0, \sigma)$ with different standard deviations. The former represents a possible inaccuracy from machine and the latter stands for both the estimate noise and the nonlinear term in the model. In the following two parts, capacity tracking and prediction implement this algorithm. The results are compared with the raw capacity calculation.

3.3.3 Tracking and Prediction

Experimental Capacity Versus Simulated Capacity Without PF

The following curves show the measured capacity combined with calculated capacity without utilization of particle filter method.

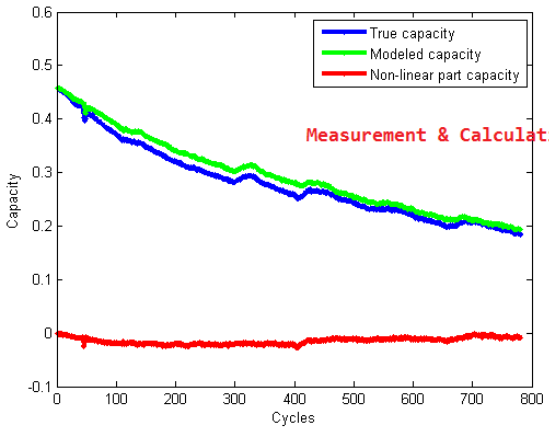

Figure 3.3: Coin KS-15 CE 1

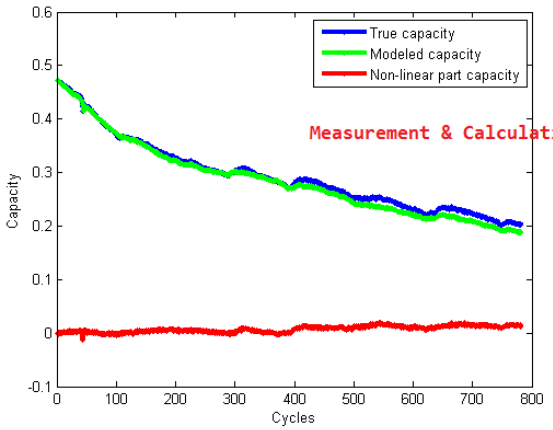

Figure 3.4: Coin KS-15 CE 2

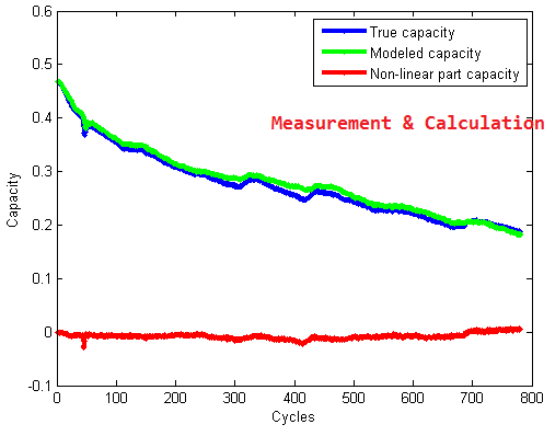

Figure 3.5: Coin KS-15 CE 3

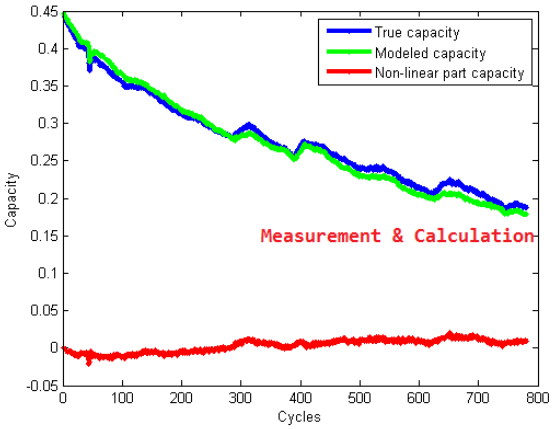

Figure 3.6: Coin SFG-6 CE 1

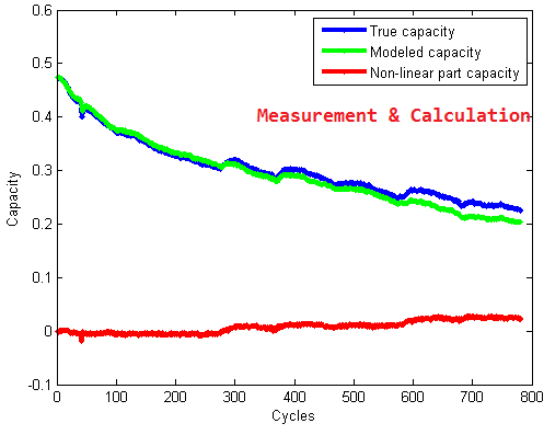

Figure 3.7: Coin SFG-6 CE 2

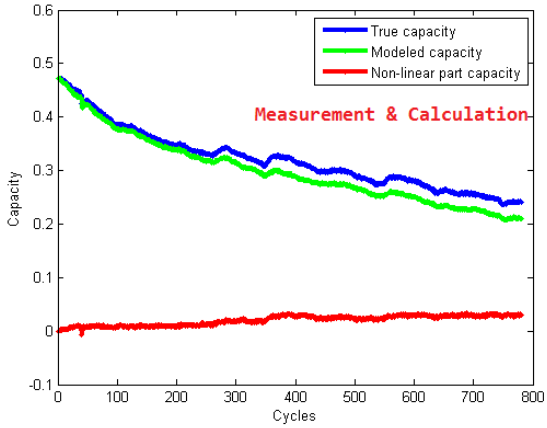

Figure 3.8: Coin SFG-6 CE 3

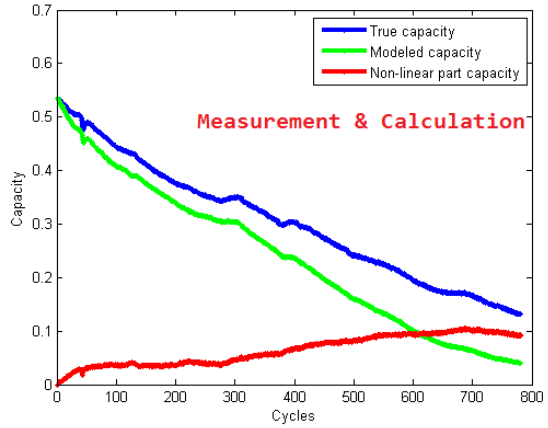

Figure 3.9: Swagelok KS-15 CE 1

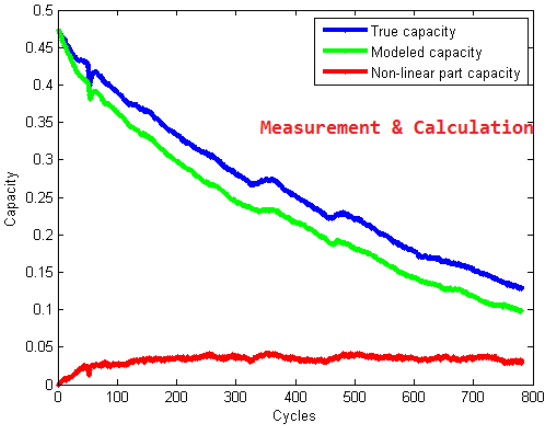

Figure 3.10: Swagelok KS-15 CE 2

In the graphs, three curves separately denote the experimental measured capacity, the raw calculated evolved capacity, and the difference between measured capacity and calculated capacity (nonlinearity term). The capacity calculation simply obeys the relationship from the model, which is $C_{k+1} = \eta_{C,k} C_k$. All the graphs obviously illustrate the similar trend between experimental data and calculated data. In terms of the individual batch of battery cells, experiment and calculation data from coin cell assembly method with either

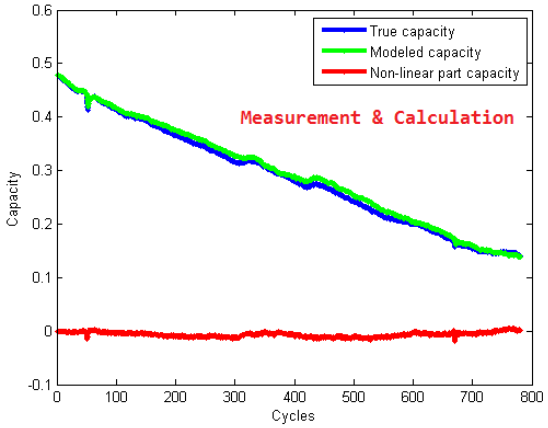

Figure 3.11: Swagelok KS-15 CE 3

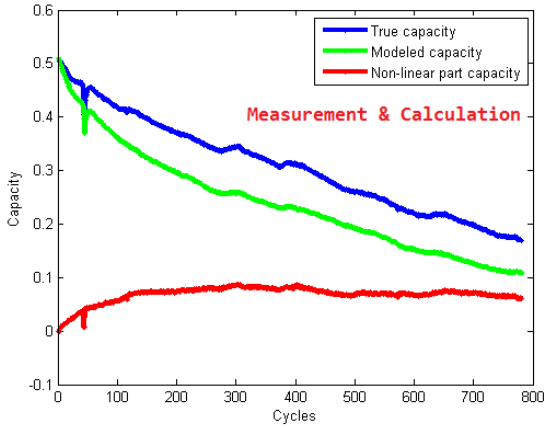

Figure 3.12: Swagelok SFG-6 CE 1

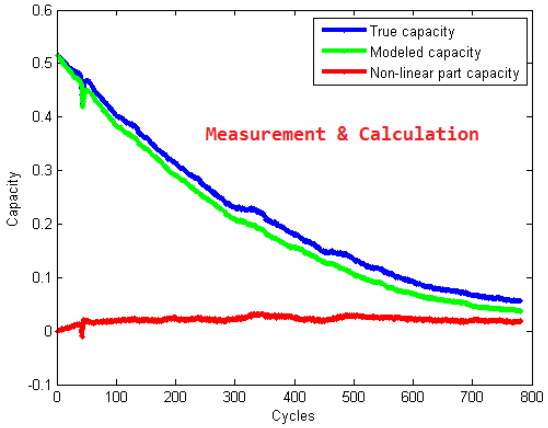

Figure 3.13: Swagelok SFG-6 CE 2

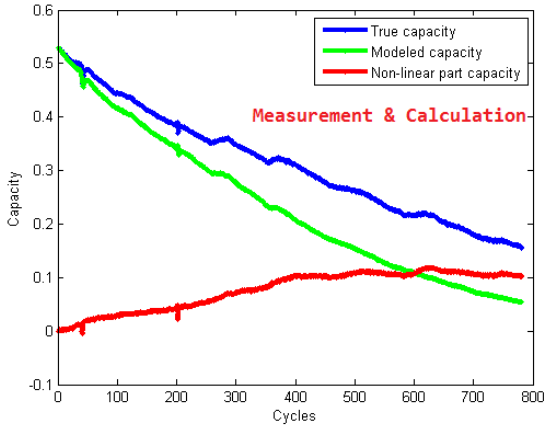

Figure 3.14: Swagelok SFG-6 CE 3

KS-15 carbon conductor or SFG-6 carbon conductor are almost the same. In another word, the nonlinear term from the model is approximately equal to zero. But for the data from Swagelok assembly cell, the true measurement is always larger than the calculated data. This small difference can be explained from the resting time when the capacity regains the capacity loss during the charge or discharge. And this difference is the nonlinear term implemented in the particle filter model.

Experimental Capacity Versus Simulated Capacity With PF Tracking

Next particle filter method is implemented as a tracking method. 100 particles are used in all the particle filter simulation. The same relationship from Coulombic efficiency and cell capacity is used in the particle filter estimation function, while the nonlinear term is covered inside the noise of the estimation during simulation. The standard deviation σ is adjusted based on the specific battery cell.

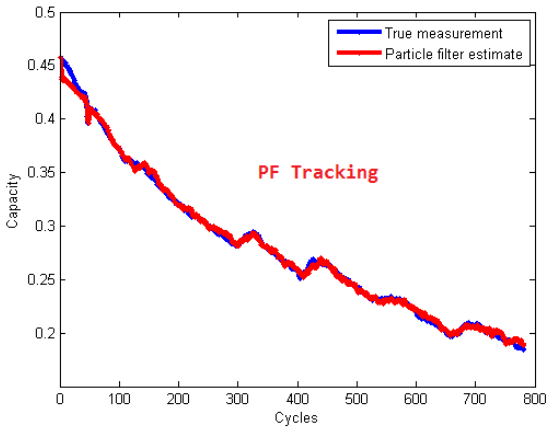

Figure 3.15: Coin KS-15 PF 1

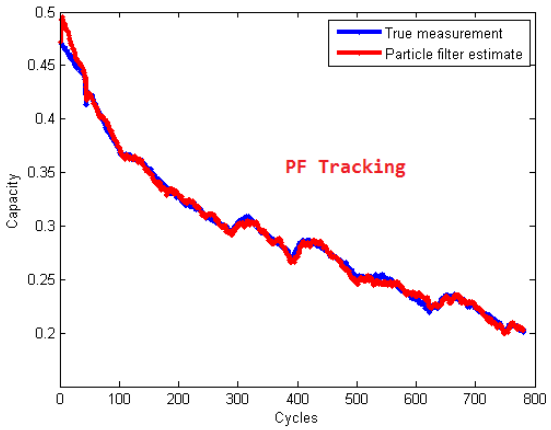

Figure 3.16: Coin KS-15 PF 2

From the graph, particle filter accurately tracks the battery capacity up to cycle 800. This is partially due to the fact that the trend of fading model is similar to the trend of real experimental data. Also particle filter method is very robust in the nonlinear calculation.

Experimental Capacity Versus Simulated Capacity With PF Prediction

Lastly, particle filter method is executed to predict the cell capacity beyond 300 cycles until 800 cycles. Experiments have confirmed that regardless of sudden severe side-reactions or a sudden battery death, the Coulombic efficiency remains at a constant value near 1 with little fluctuations. In this paper, Coulombic efficiency is averaged from the 50 cycles previously, and is used as the fixed Coulombic efficiency in the particle filter method for prediction. The model noise ω in terms of nonlinear part is adjusted and optimized from

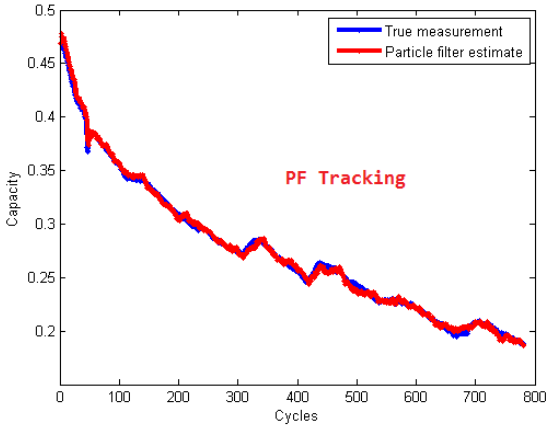

Figure 3.17: Coin KS-15 PF 3

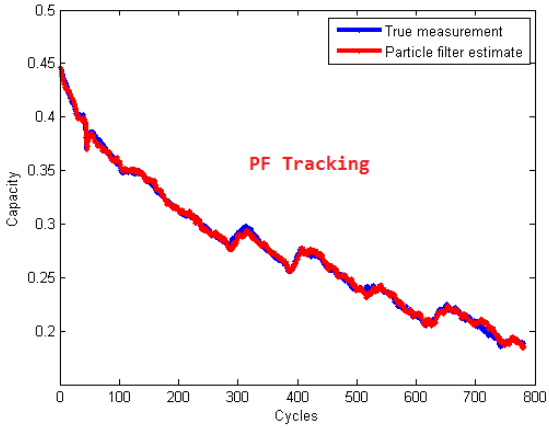

Figure 3.18: Coin SFG-6 PF 1

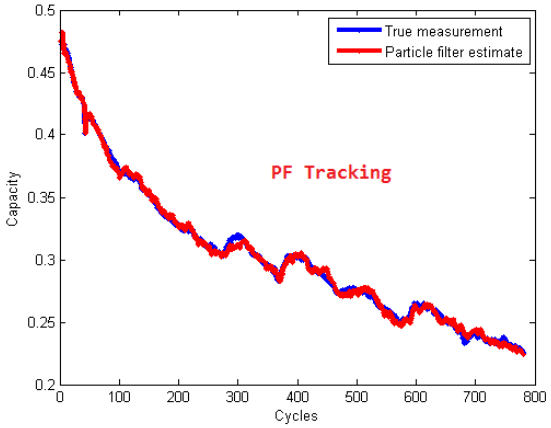

Figure 3.19: Coin SFG-6 PF 2

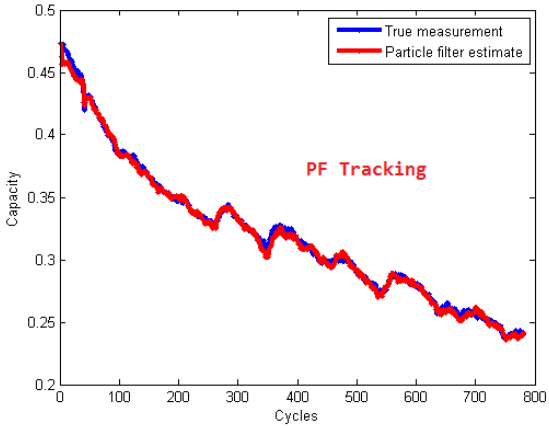

Figure 3.20: Coin SFG-6 PF 3

the first 300 cycles fitting results, which is also used in the prediction. The flow chart in Fig 3.27 shows how particle filter method is implemented for the capacity prediction.

Even though small deviations exist in the cycle capacity prediction, particle filter modeling result converges around the true measurement.

The capacity difference from modeled results and true measurement at cycle 500 is recorded in the table below. It includes raw Coulombic efficiency calculation data, particle

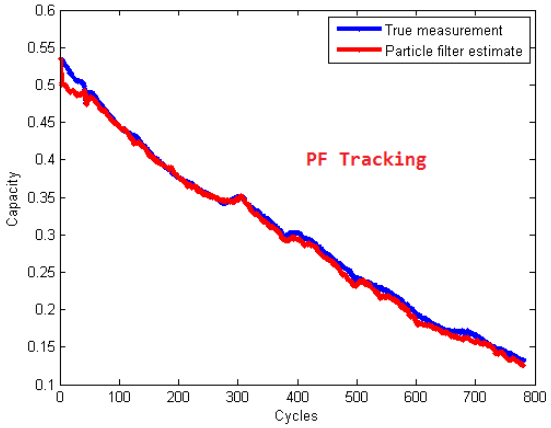

Figure 3.21: Swagelok KS-15 PF 1

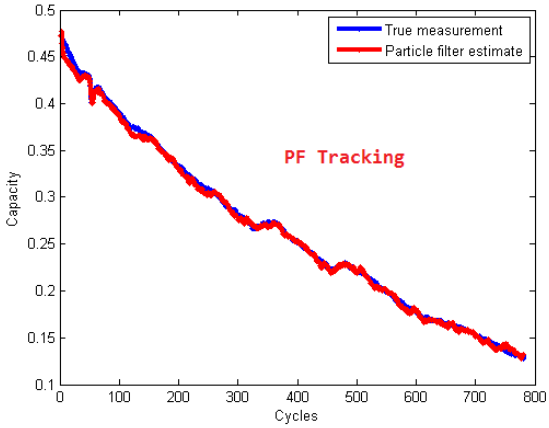

Figure 3.22: Swagelok KS-15 PF 2

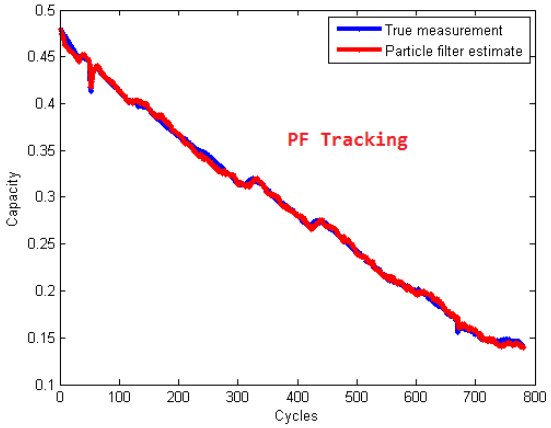

Figure 3.23: Swagelok KS-15 PF 3

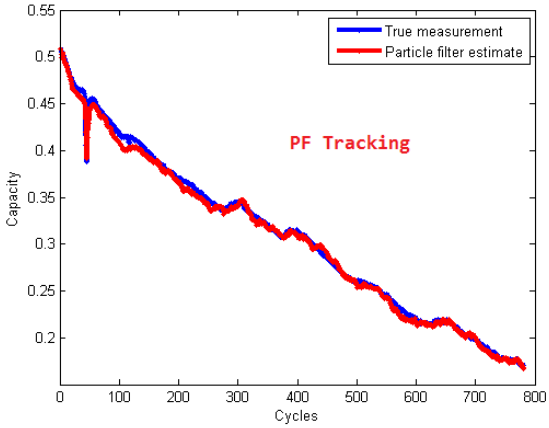

Figure 3.24: Swagelok SFG-6 PF 1

filter tracking data and particle filter prediction data.

All the results from the table show that particle filter tracking has the fittest data compared with the real experimental data. Because tracking is a direct and entire implementation of particle filter method, and it shows the advantage of particle filter method dealing with nonlinearity. In terms of calculation data and prediction data, the comparisons are not clear. Since the curves from Graph 3.3 to Graph 3.8 find that the nonlinearity

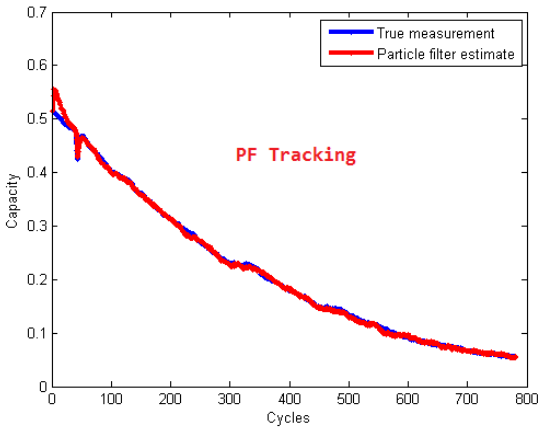

Figure 3.25: Swagelok SFG-6 PF 2

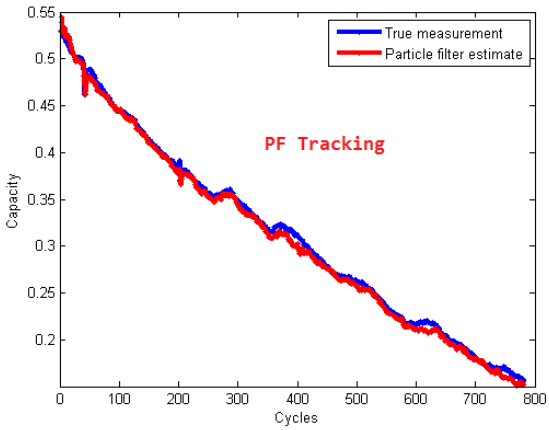

Figure 3.26: Swagelok SFG-6 PF 3

Table 3.5: Coin Cell and KS-15

CE Calculation[mAh]	PF Tracking[mAh]	PF Prediction[mAh]
0.011403	0.002758	0.009095
0.011877	0.006908	0.02818
0.008185	0.004963	0.008859

Table 3.6: Coin Cell and SFG-6

CE Calculation[mAh]	PF Tracking[mAh]	PF Prediction[mAh]
0.011686	0.007204	0.015855
0.010732	0.000354	0.009743
0.023743	0.000717	0.035757

is very small in the Coin-cell case, while the curves from Graph 3.9 to Graph 3.14 show the nonlinearity is large in the Swagelok-cell case. Moreover, the prediction only implements the first 300 cycles tracking, and it is likely that the Coulombic efficiency also fluctuates at the high cycles.

From the tables, it can also be observed that the good effect of particle filter method is more pronounced in the case of Swagelok battery data, which are generally more fluctuating

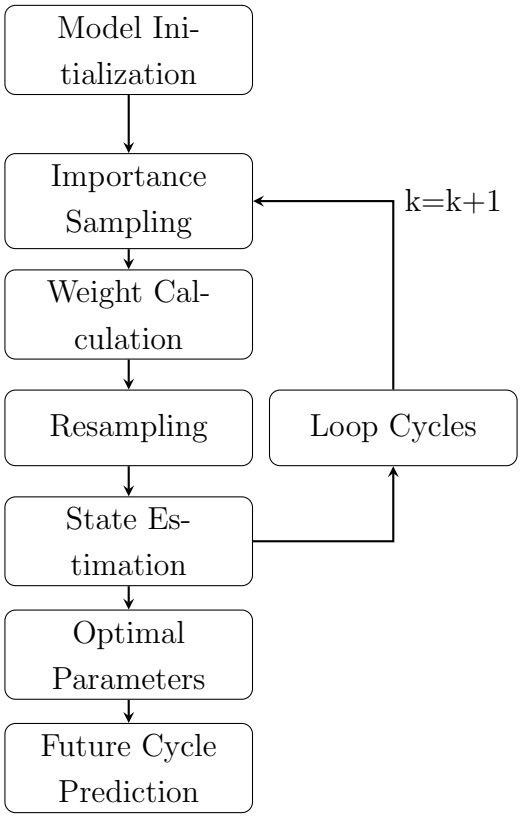

Figure 3.27: Flow Chart of Prediction Implementation

Table 3.7: Swagelok Cell and KS-15

CE Calculation[mAh]	PF Tracking[mAh]	PF Prediction[mAh]
0.082427	0.009357	0.014512
0.039052	0.000438	0.01454
0.012754	0.000049	0.020823

than coin cell data. Coin cell data are generally more stable since the batteries were pressed by machine up to a pre-set pressure. However, by modeling of data from both types of batteries, we found that the particle filter method is highly flexible, and it can work effectively with non-ideal data.

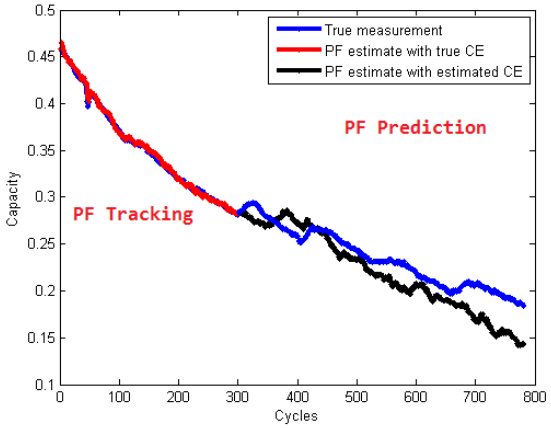

Figure 3.28: Coin KS-15 Est 1

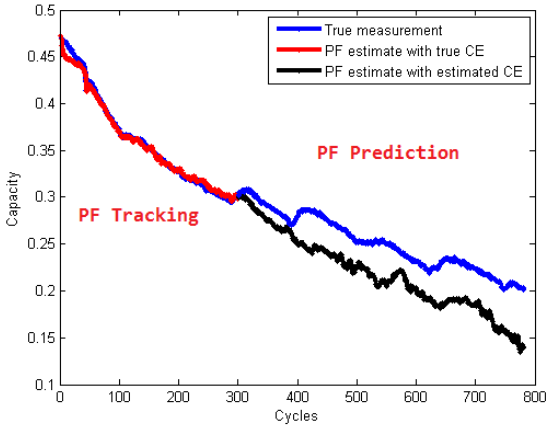

Figure 3.29: Coin KS-15 Est 2

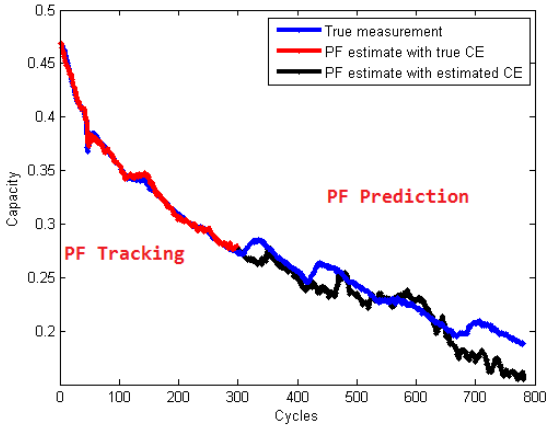

Figure 3.30: Coin KS-15 Est 3

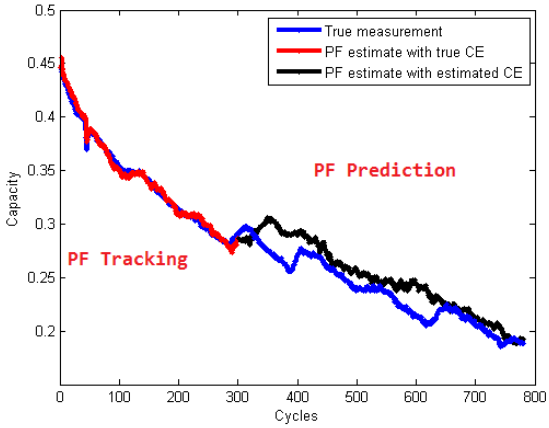

Figure 3.31: Coin SFG-6 Est 1

Table 3.8: Swagelok Cell and SFG-6

CE Calculation[mAh]	PF Tracking[mAh]	PF Prediction[mAh]
0.06635	0.002435	0.011357
0.028229	0.003838	0.022579
0.107295	0.003324	0.074672

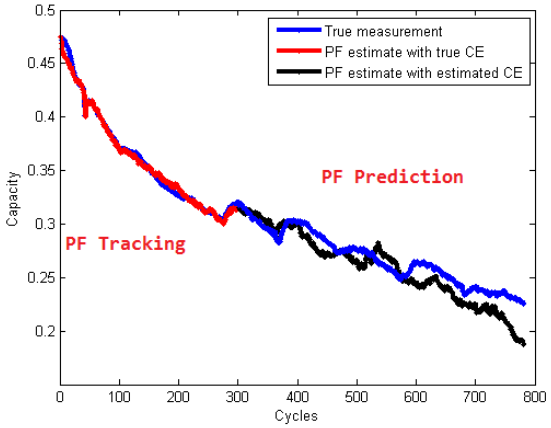

Figure 3.32: Coin SFG-6 Est 2

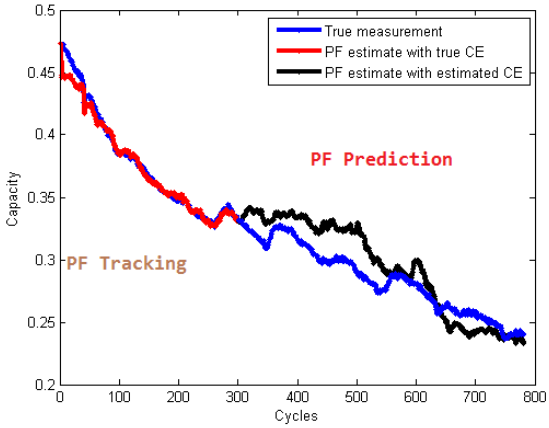

Figure 3.33: Coin SFG-6 Est 3

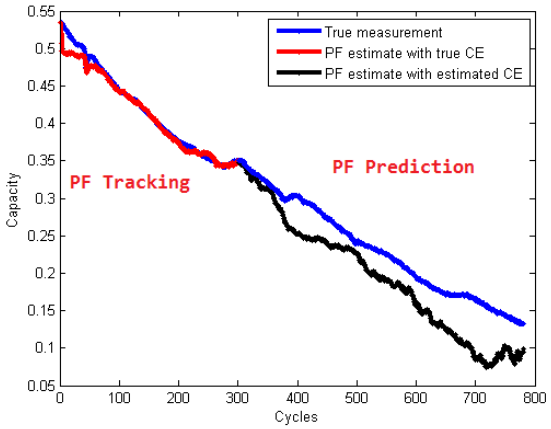

Figure 3.34: Swagelok KS-15 Est 1

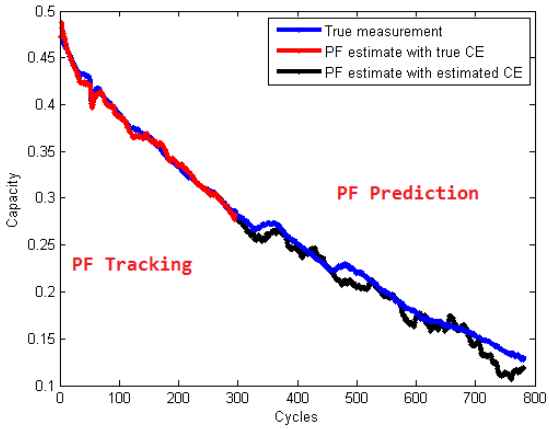

Figure 3.35: Swagelok KS-15 Est 2

3.4 Conclusion

Cycling performance of ReHABs has been experimental studied and modeled by particle filter method. The results propose that particle filter method may be an exceptional tool for both tracking and predicting the battery performance. The difference in tracked data and experimental ones is as small as 0.000049[mAh]. Futhermore, the error of predicted data is as low as 0.074672[mAh] comparing to the calculation error of 0.107295[mAh]. This

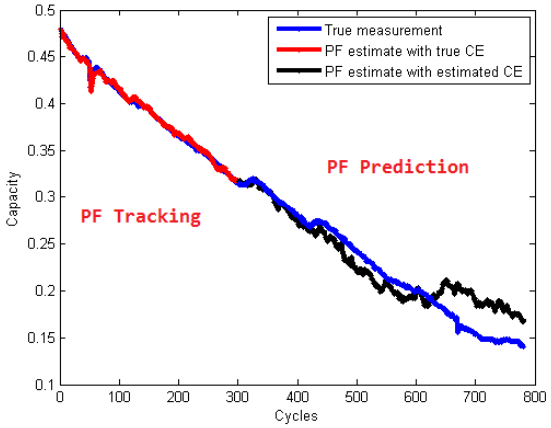

Figure 3.36: Swagelok KS-15 Est 3

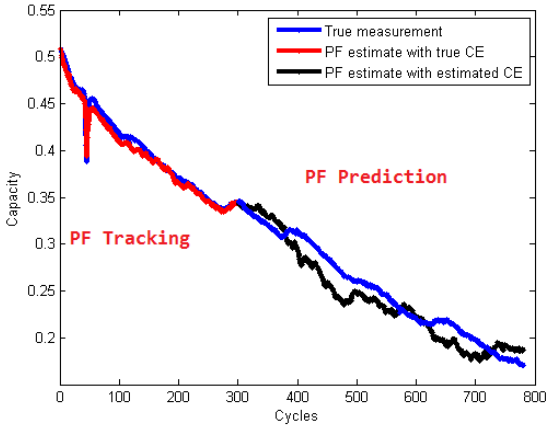

Figure 3.37: Swagelok SFG-6 Est 1

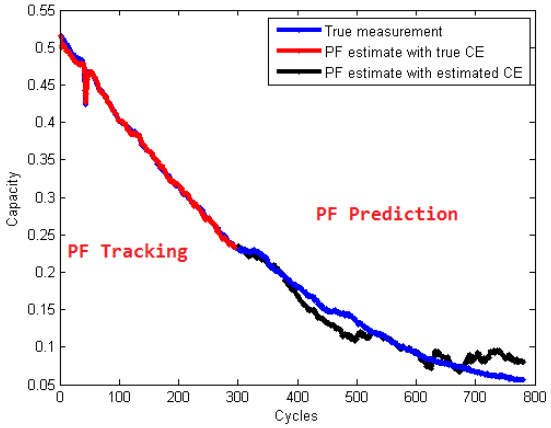

Figure 3.38: Swagelok SFG-6 Est 2

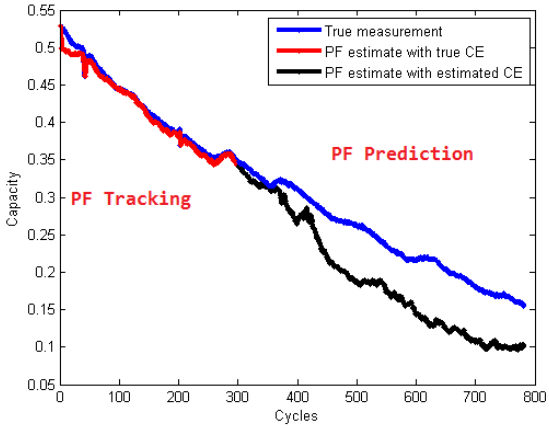

Figure 3.39: Swagelok SFG-6 Est 3

great advance may add valuable and reliable output about battery cyclability exclude the need of running batteries till the end of lives.

Chapter 4

Electrochemical Engineering Models

4.1 Cathode Study

4.1.1 Introduction

Lithium-ion battery modeling was initially attempted in the Newman's research group [36]. It established the basic theory for the future development of lithium-ion battery pseudo-2D first principle models. A set of equations is used to describe how lithium ions are intercalated in or de-intercalated from the porous electrode during discharge or charge. Meanwhile it also clarifies the connection between lithium-ion concentration and the exchange current density.

Equation Set Explanation

Two phases exist in the model by assumption. They are solid phase and liquid phase, representing electrode and electrolyte separately. Two phases are superposed between each other. In this thesis, subscript 's' means solid phase, and subscript 'l' means liquid phase. For example,

- ϕ_s Solid phase potential

- ϕ_l Solution potential
- σ_s Ion conductivity in the solid electrode
- σ_l Ion conductivity in the solution electrolyte

The model incorporates one dimensional and two dimensional scales of study. In the one dimension domain, each point on the line comprises potential or ion concentration; while in the two dimension domain, ions can transfer within a control volume.

The electrode material is considered as a spherical particle, meaning the interfacial area of the porous electrode can be calculated by

$$a_s = N_p(4\pi r_s^2) \tag{4.1}$$

The volume fraction of the solid phase ϵ_s, is given as

$$\epsilon_s = N_p(\frac{4}{3}\pi r_s^3) \tag{4.2}$$

a_s is equal to the surface area of each sphere. The fraction of solid material ϵ_s, is equal to the volume per sphere times the number of spheres per unit volume N_p. From previous two equations, one can derive:

$$a_s = \frac{3\epsilon_s}{r_s} \tag{4.3}$$

Based on the porous electrode theory, the current density of the electrolyte phase in the electrode scale (liquid in the solid) is described by Ohm's Law [17]:

$$i_l = \nabla \cdot [-\sigma_l \nabla \phi_l + \frac{2\sigma_l RT}{F}(1 + \frac{\partial \ln f}{\partial \ln c_l})(1 - t_+)\nabla \ln c_l] \tag{4.4}$$

Thus the current density in the solid phase of the electrode is

$$i_s = I - i_l = -\sigma_s \nabla \phi_s \tag{4.5}$$

where I denotes the current density. This is based on the assumption that the divergence of the total current density is zero.

Meanwhile, the mass balance of lithium-ion in the electrode can also give

$$\epsilon_s^{eff}\frac{\partial c_l}{\partial t} + \nabla \cdot N_l = R_l \tag{4.6}$$

The first term on the left represents the concentration change with respect to time. The second term on the left means the flux of the lithium-ion, which can be further obtained by the addition of species diffusion and convection. And the last term shows any possible reaction that can influence the concentration of lithium. In the expansion of the flux term N_l,

$$N_l = -D^{eff}\nabla c_l + \frac{i_l t_+}{F} \tag{4.7}$$

From the Bruggeman relation, the effective diffusivity coefficient D^{eff} and effective solid conductivity coefficient are related to solid phase fraction ϵ_s.

$$\sigma_s^{eff} = \sigma_s \epsilon_s^{1.5} \qquad D^{eff} = D_s \epsilon_s^{1.5} \tag{4.8}$$

At the pure solid phase of microscopic scale, the process of lithium-ion intercalation/de-intercalation is treated as a diffusion process. It follows the second Fick's Law in the spherical coordinate that

$$\frac{\partial c_s}{\partial t} = \nabla \cdot (D_s \nabla c_s) = D_s \frac{\partial^2 c_s}{\partial r^2} + \frac{2D_s}{r}\frac{\partial c_s}{\partial r} \tag{4.9}$$

The boundary condition is,

$$\frac{\partial c_s}{\partial r} = 0, \quad r = 0 \tag{4.10}$$

$$j_n = \frac{i_n}{F} = -D_s \frac{\partial c_s}{\partial r}, \quad r = R_s \tag{4.11}$$

Here, R_s is the particle radius, c_s denotes the solid phase concentration of lithium-ions in the particles. At the surface of a particle, the solid concentration of lithium-ion corresponds to the solid phase concentration c_s in the electrode scale. The surface flux of lithium-ion j_n is equal to the particle ion diffusion at the surface.

The interfacial kinetics is expressed in the dependence of the local electrochemical reaction rate on the concentration and potential. The most famous equation, Butler-Volmer equation is,

$$i_n = i_0[\exp(\frac{\alpha_a F\eta}{RT}) - \exp(-\frac{\alpha_c F\eta}{RT})] \tag{4.12}$$

i_n refers to the local current density during charge or discharge. η, which is defined as overpotential, is expressed as $\eta = \phi_s - \phi_l - E_{eq}$. E_{eq} is the equilibrium open circuit potential. The exchange current density i_0 is [36]

$$i_0 = F(k_c)^{\alpha_a}(k_a)^{\alpha_c}(c_{max} - c_s)^{\alpha_a}(c_s)^{\alpha_c}(\frac{c_l}{c_{c,ref}})^{\alpha_a} \tag{4.13}$$

where α_c and α_a, representing cathode and anode specific characteristic number, are usually identified as 0.5.

Lastly, the charge balance relating local current density i_n and the divergence of the current to the surface diffusion flux j_n is

$$ai_n = aFj_n = \nabla \cdot i_l \tag{4.14}$$

All the equations listed above are supposed to be solved using numerical methods. COMSOL Multiphysics finite element solver includes six unknown, which are the concentration in the solid electrode phase c_s, liquid electrolyte phase c_l, the solid phase potential ϕ_s, liquid phase potential ϕ_l, the electrolyte phase current density i_l, and the local current density i_n. Further details can also be added into the model such as side reactions or thermal effects.

Time dependent solver is used in the study. Initial conditions and boundary conditions should be formalized at first. Then the time stepping moves on until the cut-off voltage or cut-off current is reached.

Side Reaction

$LiMn_2O_4$ has been identified as unstable at the end of discharge, when Mn^{3+} is highly concentrated. The possible mechanism is denoted as the self-discharge of $LiMn_2O_4$. Mn^{3+}

is very likely to be converted to Mn^{2+} and Mn^{4+}.

$$2Mn^{3+} \longrightarrow Mn^{2+} + Mn^{4+} \tag{4.15}$$

By analysis, the side reaction becomes serious when the cathode is at the end of the discharge. This study proposes a side reaction expression depending on the potential.

$$i_{side} = -i_{0,side} \exp(\frac{-0.5F\eta}{RT}) \tag{4.16}$$

The negative sign compared with the current direction of the discharge is rendered to give a negative influence to the battery performance. $i_{0,side}$ is the exchange current density of the side reaction.

4.1.2 Results and Discussion

General Discharge Curve

The material properties chosen for the model are obtained from COMSOL battery module [18]. The anode material is Zn and the cathode material is $LiMn_2O_4$. Zn equilibrium potential is set as -0.763V. Based on the literature, the equilibrium potential of $LiMn_2O_4$ versus the state of charge is [36]

$$U = 4.19829 + 0.0565661 \tanh[-14.5546y + 8.60842] - 0.0275479[\frac{1}{(0.998432 - y)^{0.492465}} - 1.90111] - 0.157123 \exp(-0.04738y^8) + 0.810239 \exp[-40(y - 0.133875)] \tag{4.17}$$

where y is the amount of lithium inserted in $Li_yMn_2O_4$. This potential is recorded with respect to lithium equilibrium potential (Li is -3.0401V relative to standard hydrogen electrode). The curve in Graph 4.1 illustrates the $LiMn_2O_4$ equilibrium potential.

The curves in Graph 4.2, Graph 4.3 and Graph 4.4 show simulated battery discharge, lithium ion concentration in the electrolyte in the porous electrode domain and lithium-ion concentration at the cathode electrode surface.

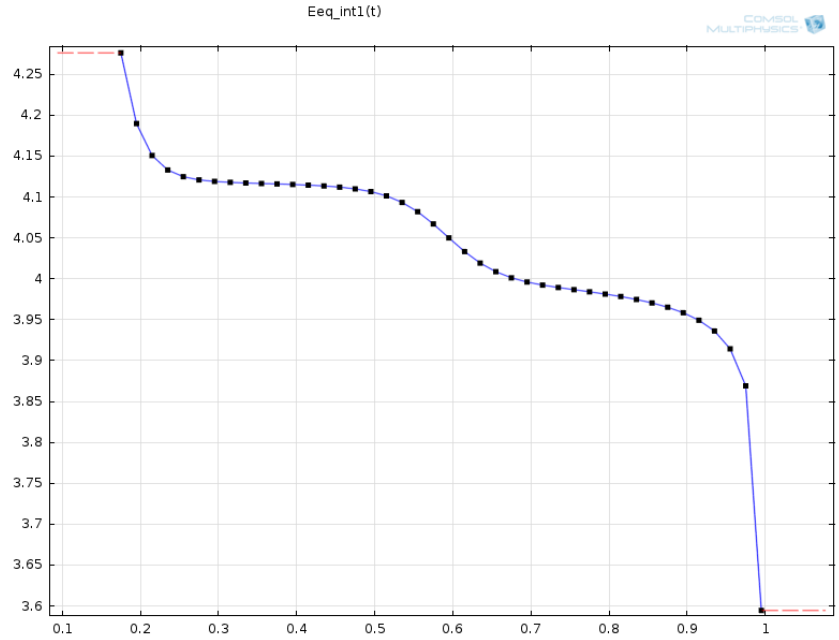

Figure 4.1: Equilibrium Potential of $LiMn_2O_4$

Equilibrium potential (open circuit potential) of $LiMn_2O_4$ as a function of the state of charge relative to solid lithium. x-axis represents the state of charge/discharge, and y-axis represents the potential versus Li/Li^+ equilibrium potential.

From the simulation graphs, the discharge process starts at around 1.95V and ends at around 1.55V. The truncation is the result when most lithium insertion sites in $LiMn_2O_4$ are occupied. In terms of concentration changes during discharge, at the electrolyte domain, the lithium ion concentration increases. The increment becomes bigger towards the direction of the current collector site (the cathode ending point). At the electrode domain, lithium ion concentration at the particle surface also increases during discharge. It reaches the maximum when time arrives at 3000s defined in the simulation. These findings are consistent with the theoretical analysis of the lithium-ion battery discharge process. During the discharge, lithium ions are intercalated into the electrode. This causes increased ion concentration in the liquid electrolyte inside the porous electrode; meanwhile, the surface ion concentration is supposed to be increased due to the ion insertion.

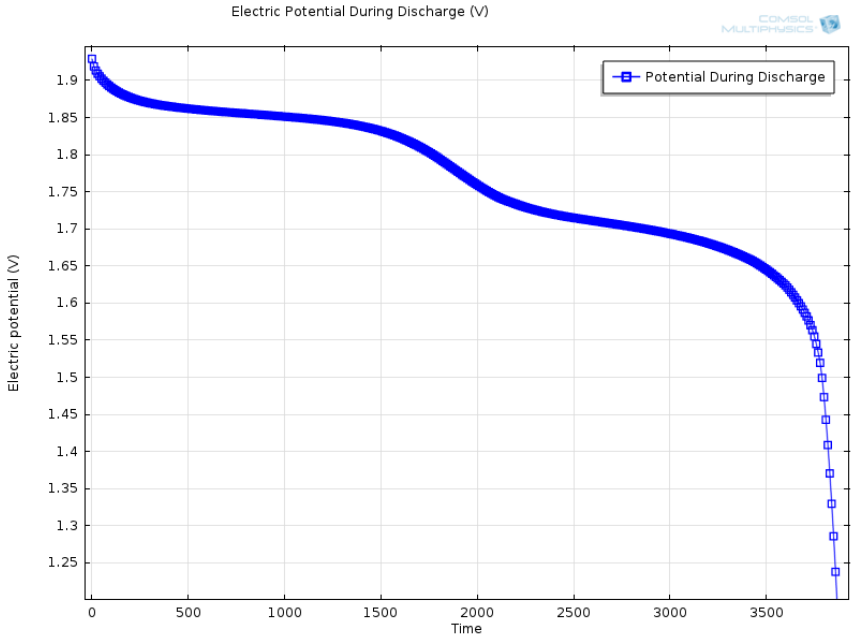

Figure 4.2: $LiMn_2O_4$ Discharge Curve

$LiMn_2O_4$ discharge curve vs time in the simulation. The operational potential is around 1.55V to 1.95V from the simulation. x-axis represents the simulation time (s), and y-axis represents the operational potential (V).

Constant-current and Constant-voltage

Constant-current and constant-voltage (CC-CV) tests are applied in the simulation over 100 cycles. Events interface inside COMSOL helps define the details. The procedure of CC-CV test is conditioned such that,

- Constant-current charge: $i_{app} = i_{ch}$
- Constant-voltage charge: $E_{cell} = E_{cell,max}$
- Resting time: $i_{app} = 0$
- Constant-current discharge: $i_{app} = i_{dch}$

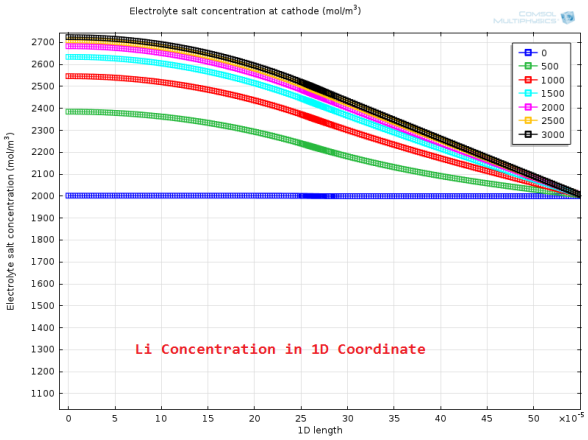

Figure 4.3: Lithium Ion In Electrolyte
x-axis represents the x-coordinate in the simulation, and y-axis represents the Li^+ concentration in the electrolyte in the porous electrode domain.

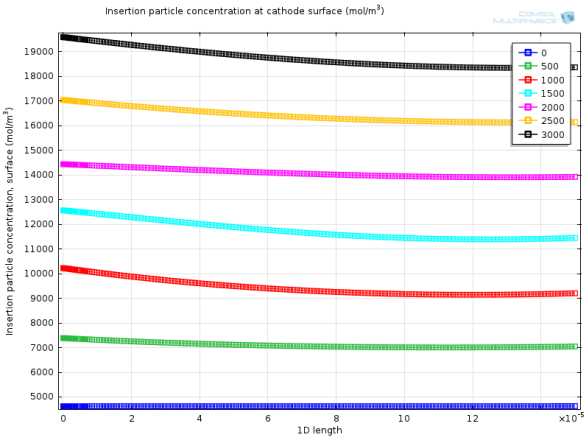

Figure 4.4: Lithium Ion At Particle Surface
x-axis represents the x-coordinate in the simulation, and y-axis represents the Li^+ concentration in the $LiMn_2O_4$ particle surface.

- Constant-voltage discharge: $E_{cell} = E_{cell,min}$
- Resting time: $i_{app} = 0$

i_{ch} is the constant charging current (A/m^2), E_{cell} is the battery cell voltage (V), $E_{cell,max}$ is the maximum voltage limit of constant charging when cell starts constant-voltage (V), i_{dch} is the constant discharging current (A/m^2), $E_{cell,min}$ is the minimum voltage limit of constant discharging when cell starts constant-voltage (V). The testing is shown in the Graph 4.5 below.

A side reaction term is added into the CC-CV mode for cycles to observe the potential at cycle 1, 10, 50, 100. The exchange current density is set as 1.5e-2(A/m^2), which is assumed to have some side-effects compared with 0.08(mA/cm^2) for $LiMn_2O_4$ exchange current density [37]. The first graph in Figure 4.6 shows the experimental result [7]. The second two graphs in Figure 4.7 and Figure 4.8 show the simulation results.

From the results, both charge and discharge processes have a gradual voltage decrease with the increase of the cycle number. In Figure 4.7 and Figure 4.8, both cell voltages slowly drop from cycle 1, cycle 10, cycle 50, and until cycle 100. This is due to the side reaction

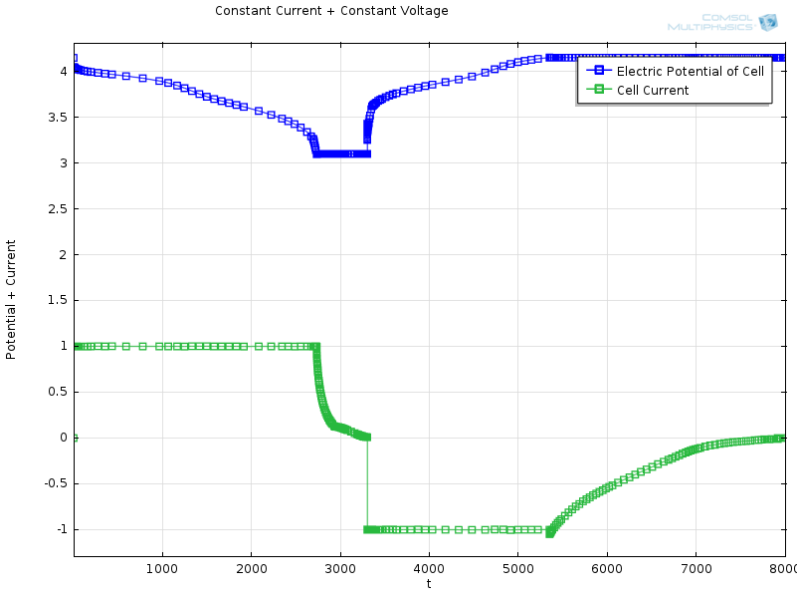

Figure 4.5: Constant-current Constant-voltage
The upper curve shows cell voltage during CC-CV, and the lower curve shows cell current density during CC-CV. x-axis represents the time (s) in the simulation, and y-axis represents voltage (V) and current (A) separately.

set inside the simulation. This proposed term causes a similar phenomena observed in the experiment during discharge process, since from Figure 4.6, the voltage drops clearly from cycle 1 to cycle 1000. But in terms of charge process, the voltage gradually increases in the experiment. It is explained from the experimental view that the side reaction expands the gap between the charge voltage and discharge voltage curves. Thus the model needs more adjustments in the future study.

4.1.3 Conclusion

To sum up, this model successfully simulates $LiMn_2O_4$ cathode with the lithium-ion battery interface. Compared with the real battery discharge curves, the simulated discharge results not only exhibit similar curves, but also illustrate the Li distribution in the active

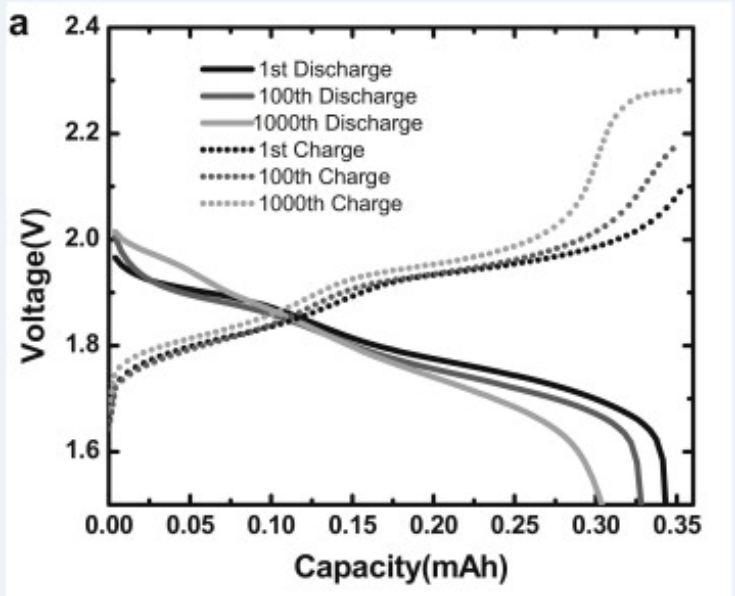

Figure 4.6: Experimental Charge/Discharge Curves

Experimental charge/discharge potential profiles.

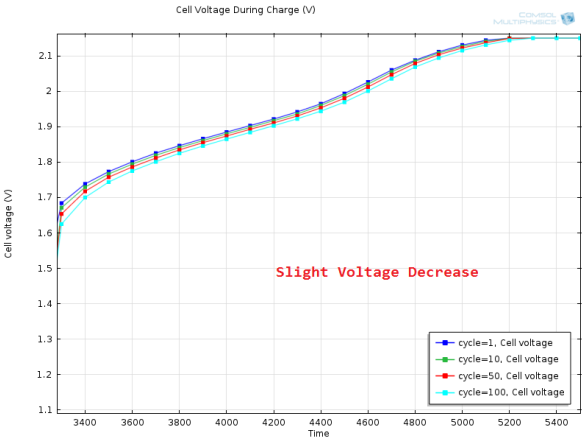

Figure 4.7: Simulation Charge Profile

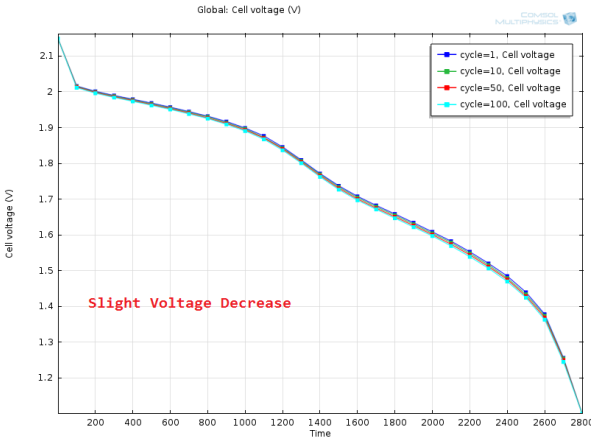

Figure 4.8: Simulation Discharge Profile

material particle phase and electrolyte phase. This illustration explains that Li concentration increases during discharge at the cathode. Furthermore, the model incorporates a

side-reaction term in the constant-current constant-voltage battery test. This term causes a gradual battery voltage decrease during charge and discharge. This finding is consistent with the experimental data in terms of discharge process, but modifications are required since the charge process in the experiment shows different trend compared with the model.

4.2 Zinc Study

4.2.1 Introduction

In the ReHABs, the main processes at the anode are the dissolution of Zn during discharge and deposition of Zn^{2+} during charge. The Zn surface is chemically corroded by reactions with the acidic electrolyte media and electrochemically corroded by the operation near H_2 evolution potential, which leads to H_2 evolution. A clear understanding about the thermodynamics and kinetics of such processes is important for experimental designs. This part is focused on a mathematical study of chemical reactions on Zn in contact with electrolyte.

4.2.2 Model Definition

Nernst-Planck Interface

Transport process is mainly considered to describe the kinetic process. There are basically two transport processes happening, species diffusion and migration. Based on the Fick's Law, the diffusion flux of species i flows can be represented as,

$$\vec{J_i} = -D_i \nabla c_i \tag{4.18}$$

where $\vec{J_i}$ denotes the flux of ions per unit area, D_i is the diffusion coefficient, and the concentration gradient ∇c_i gives rise to the driven force of diffusion. In the non-steady state of diffusion, the process can be further given as

$$\frac{\partial c_i}{\partial t} = -D_i \nabla^2 c_i \tag{4.19}$$

Migration is another transport process driven by the potential gradient. The velocity of the species i is expressed as

$$\vec{v_i} = -u_i \nabla \mu_i \tag{4.20}$$

where u_i is the mobility. The flux thus takes the form

$$\vec{J_i} = c_i \vec{v_i} = -u_i c_i \nabla \mu_i = -\frac{D c_i}{RT} \nabla \mu_i \tag{4.21}$$

Here R is the universal gas constant. The diffusion coefficient $D_i = u_i RT$ is based on Einstein relation. The potential gradient originates from changes in composition and electric potential ϕ, thus

$$\nabla \mu_i = RT \nabla \ln c_i + z_i F \nabla \phi \tag{4.22}$$

in which F is the Faraday constant and z_i is the charge number of the species. Assuming the composition does not change during operation, the total flux from diffusion and migration is

$$\vec{J_i} = -D_i(\nabla c_i + \frac{z_i c_i F}{RT} \nabla \phi) \tag{4.23}$$

The first term on the right, denoted as diffusion flux, is the result of random thermal motion of the species. The second term as migration, is the effect exerted by local electrical field. This is the so-called Nernst-Planck equation, a description of mass conservation under the influence of ionic concentration gradient and electrical potential distribution. The role of migrational term is to ensure that the solution remains as electroneutrality. If there are some chemical reactions, the total transport expression on the change of the species concentration is given as

$$\frac{\partial c_i}{\partial t} = D_i \nabla^2 c_i + \frac{z_i D_i F}{RT} \nabla (c_i \nabla \phi) + R_i \tag{4.24}$$

where R_i is the rate of production or depletion of species i.

Thermodynamic Relations

Equilibrium Potential Thermodynamic relation is originated from the consideration of energy relations. The tendency of a chemical reaction can be explained by Gibbs free energy G. The change of free energy, which is ΔG, is denoted by the difference between products and reactants.

$$\Delta G = \sum_i \mu_{i,prod} - \sum_i \mu_{i,rect} \tag{4.25}$$

In the standard conditions (partial pressure of gas in the reaction is 0.1MPa, concentrations of all aqueous solutions are 1M), the standard free energy change ΔG^0 is used to illustrate the tendency of a chemical reaction. It is defined that if $\Delta G^0 < 0$, the reaction

is happening spontaneously; if $\Delta G^0 > 0$, the inverse reaction proceeds spontaneously; and if $\Delta G^0 = 0$, the reaction is in the state of equilibrium. If a chemical reaction is written as $\mathrm{aA} + \mathrm{bB} \rightleftharpoons cC$, the equilibrium constant K of the reaction is defined as

$$K = \frac{\alpha_C^c}{\alpha_A^a \cdot \alpha_B^b} = \frac{\text{Product of activities of products}}{\text{Product of activities of reactants}} \tag{4.26}$$

Given the standard-state free energy of a reaction expressed as $\Delta G^0 = -RT \ln K$ and the relationship between free energy change ΔG with electrochemical reaction driving force,

$$\Delta G = -nFE \qquad \Delta G^0 = -nFE^0 \tag{4.27}$$

an expression is derived as

$$E = E^0 + \frac{RT}{nF} \ln[\frac{\text{Product of activities of reactants}}{\text{Product of activites of products}}] \tag{4.28}$$

where E^0 is also called standard electrode potential if explained with respect to electrochemical reaction. E is the electromotive force and nF is the total charge per molecule of ions involved in the reaction.

Electrochemical Reaction Two most important species at the anode generating electrochemical reactions are zinc and hydrogen ions. The reactions written in the standard forms are

$$\mathrm{Zn} - 2\,\mathrm{e}^- = \mathrm{Zn}^{2+} \qquad E^0 = -0.763V \tag{4.29}$$

$$2\,\mathrm{H}^+ + 2\,\mathrm{e}^- = \mathrm{H}_2 \qquad E^0 = 0.0V \tag{4.30}$$

While in terms of the real processes at the zinc side, the equilibrium potentials for two reactions are modified as

$$E_{\mathrm{Zn}} = -0.763 + \frac{RT}{2F} \ln[\frac{a_{\mathrm{Zn}^{2+}}}{a_{\mathrm{Zn}}}] \tag{4.31}$$

$$E_{\mathrm{H}_2} = 0.0 + \frac{RT}{F} \ln[\frac{a_{\mathrm{H}^+}}{(a_{\mathrm{H}_2})^{0.5}}] \tag{4.32}$$

The activity (a_i) of species Zn^{2+} and H^+ is related to the concentration (y_i) and the activity coefficient (γ_i)

$$a_i = \gamma_i y_i \tag{4.33}$$

where the activity coefficients constant are $\gamma_{Zn^{2+}} = 0.1$ and $\gamma_{H^+} = 0.5$. With the potential given at the Zn anode, the overpotential or polarization (η) for Zn and H_2 are

$$\eta_{Zn} = E - E_{Zn} \tag{4.34}$$

$$\eta_{H_2} = E - E_{H_2} \tag{4.35}$$

When the Zn process ($Zn \rightarrow Zn^{2+}$) and H^+ process ($2\,H^+ \rightarrow H_2$) are happening simultaneously, the former is working anodically while the latter is working cathodically, causing the unwanted corrosion at the Zn anode.

The polarization for an electrochemical reaction can be categorized into activation polarization and concentration polarization. The former can also be divided into cathodic polarization η_c and anodic polarization η_a depending on positive polarization or negative polarization.

$$\eta_c = \beta_c \log \frac{i_c}{i_0} \qquad\qquad \eta_a = \beta_a \log \frac{i_a}{i_0} \tag{4.36}$$

in which i_0 is the exchange current density; β_c and β_a are cathodic and anodic Tafel constant; i_c and i_a are cathodic and anodic exchange current density. In terms of concentration polarization, which is caused by the changes in the ion concentration near the electrode/electrolyte interface, happens when reaction proceeds fast. The polarization (η_{conc}) in terms of H_2 reaction, is expressed as

$$\eta_{conc} = \frac{RT}{nF} \ln \frac{[H^+]^2}{p_{H_2}} \tag{4.37}$$

Corrosion as a combination of cathodic reactions and anodic reactions is defined with respect to corrosion potential (E_{corr}) and corrosion current (i_{corr}). The kinetic expression at the metal surface is written as

$$i = i_a - i_c = i_{corr}[\exp(\frac{\eta}{\beta_a}) - \exp(-\frac{\eta}{\beta_c})] \tag{4.38}$$

where $\eta = E - E_{corr}$ is the overpotential at the metal surface; the anodic polarization $\eta_a = E - E_{corr}$ and cathodic polarization $\eta_c = E - E_{corr}$ are related to the Zn oxidation and H^+ reduction.

Kinetics

Apart from the main electrochemical reactions, there are some possible reactions happening at the anode position. These reactions not only change the species concentration in the solution, but at the same time influence the equilibrium potential of the species. For the ionic species H^+ and OH^-, the ionization of H_2O gives the rate

$$H_2O \rightleftharpoons H^+ + OH^- \tag{4.39}$$

At the same time, it is highly suspected that there are some potential reactions happening related to Zn.

$$Zn + 2\,H_2O \rightarrow Zn(OH)_2 + H_2 \tag{4.40}$$

$$Zn^{2+} + 2\,H_2O \rightleftharpoons Zn(OH)_2 + 2\,H^+ \tag{4.41}$$

In terms of H_2O reaction for example, the reaction rate based on the law of equilibrium, is

$$R_{H_2O} = k_{f,H_2O}[H_2O] - k_{b,H_2O}[H^+][OH^-] \tag{4.42}$$

The equilibrium constant of H_2O (K_{H_2O}) is $10^{-8}[mol^2m^{-6}]$ from software HSC Chemistry, and if the relationship between forward and backward rate is

$$K_{H_2O} = \frac{k_{f,H_2O}}{k_{b,H_2O}} \tag{4.43}$$

The equilibrium constants for all the reactions are referred from HSC Chemistry, while in terms of forward or backward rate, the values are found from online resources or estimated by experience [70, 71].

According to Nernst-Planck interface, the transport equations in one dimension for interested species are

$$D_{Zn^{2+}}[\frac{d^2[Zn^{2+}]}{dx^2} + \frac{2F}{RT}\frac{d}{dx}([Zn^{2+}]\frac{d\phi}{dx})] - (k_{f,Zn^{2+}}[Zn^{2+}][H_2O]^2 - k_{b,Zn^{2+}}[H^+]^2) = \frac{i_a}{2F}$$
$$D_{H^+}[\frac{d^2[H^+]}{dx^2} + \frac{F}{RT}\frac{d}{dx}([H^+]\frac{d\phi}{dx})] + 2(k_{f,Zn^{2+}}[Zn^{2+}][H_2O]^2 - k_{b,Zn^{2+}}[H^+]^2)$$
$$+ k_{f,H_2O}[H_2O] - k_{b,H_2O}[H^+][OH^-] = -\frac{i_c}{F}$$
$$D_{H_2}\frac{d^2[H_2]}{dx^2} = \frac{i_c}{2F}$$

in which i_a and i_c denote current density from Zn oxidation and H^+ reduction. The pH value of the solution is represented via H^+ concentration, which is

$$pH = -\log(0.001 \cdot [H^+]) \tag{4.44}$$

COMSOL Simulation

COMSOL Multiphysics is used to establish a one dimensional model. The model is composed of a electrochemical reaction site, a species transport region and an end representing bulk solution. Figure 4.9 shows, a linear line connecting two points defines the problem to be simulated.

The right point is illustrated as the bulk solution site, meaning there is no chemical or electrochemical reaction happening. All the concentrations are assumed to be constant at this position. The left point of the line is defined as the active reactive site, where species have electrochemical reactions and potential chemical reactions. Flux caused by species diffusion, convection and reactions gives rise to current density and changes of electric potential here. The line connecting two points is denoted as the transition region, which means there is no metal corrosion, but the species diffusion and migration happens.

COMSOL Nernst-Planck interface is implemented to investigate the process at final steady state. The domain and boundary definitions are based on what is described above. Simulation parameters are covered in the appendix.

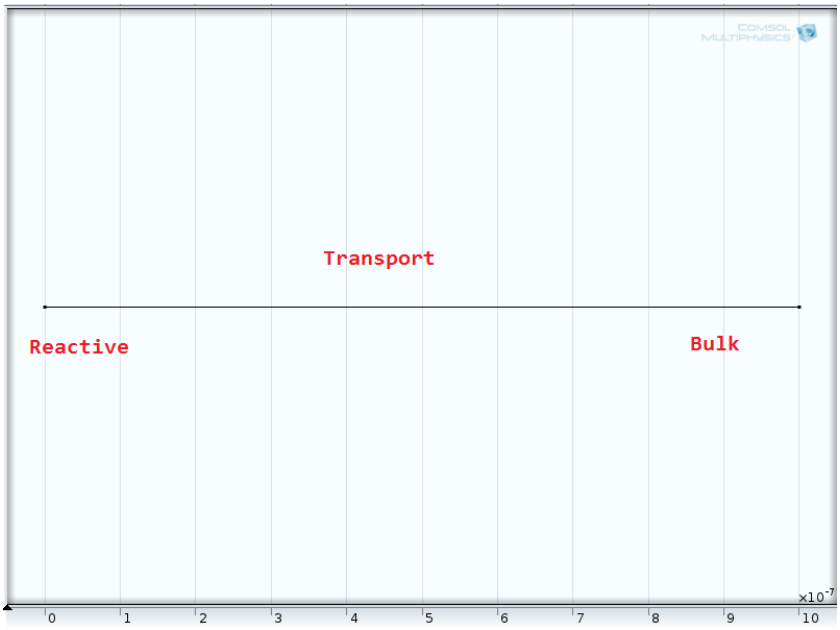

Figure 4.9: Zinc Corrosion Geometry
x-axis represents the x-coordinate in the simulation, and y-axis represents y-coordinate in the simulation. The length is set in the magnitude of 10^{-7} m for study purpose.

4.2.3 Results and Discussion

Experimental Measurement

Experiments have been done in the lab measuring Tafel curve of zinc corrosion. The pH environment is maintained at around 4. The composition of the solution is $ZnSO_4$ and Li_2SO_4 with different concentration. Figure 4.10 shows the experimental setup in Tafel test. In the Tafel test, working electrode is Zn, and the relative electrode is $Hg/HgSO_4$, whose potential is 0.654V relative to the standard hydrogen electrode.

The experimental Tafel curves with different compositions of Li_2SO_4 (1M and 2M) show some differences (-1.436V for 1M Li_2SO_4 and -1.424V for 2M Li_2SO_4). Based on the theory, the corrosion potential should not be drastically influenced by Li^+ concentration. But from the experimental results, larger Li^+ causes higher corrosion potential. It can be

Figure 4.10: Linear Polarization Studies
In the Tafel test, working electrode is Zn, and the relative electrode is $Hg/HgSO_4$, whose potential is 0.654V relative to the standard hydrogen electrode.

explained that when Li^+ is concentrated, it influences Zn^{2+} and H^+ flows. This influence might cause the equilibrium potential increment.

Simulated Result

The model uses linear cyclic voltage sweeping method to simulate the Tafel curve, meaning that it provides a sweeping voltage in a range $[V_{min}, V_{max}]$ where corrosion potential is situated inside. In the model, Zn^{2+} is initialized as 1M for the whole one-dimensional line. Two different H^+ concentration are set in the model, which are pH=3.0 and pH=4.0. After implementing the stationary Nernst-Planck interface, the model can show the final steady

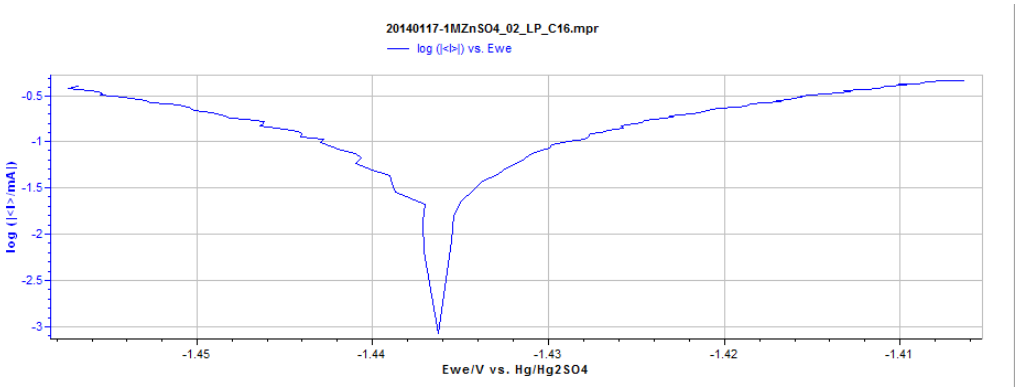

Figure 4.11: Tafel I 1M Li_2SO_4

x-axis shows the potential (V), y-axis shows the current in the logarithmic modification.

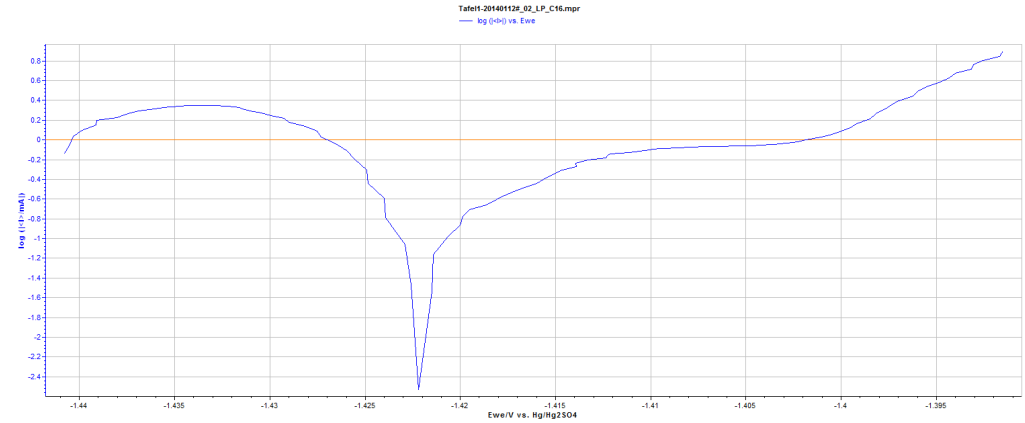

Figure 4.12: Tafel II 2M Li_2SO_4

x-axis shows the potential (V), y-axis shows the current in the logarithmic modification.

state for the system.

The results from Figure 4.14 and Figure 4.15 show that pH is almost the same as the initialization. It is because the right side of bulk solution is kept at a constant concentration. But at the left side, pH increases with a small amount, which is due to the H^+

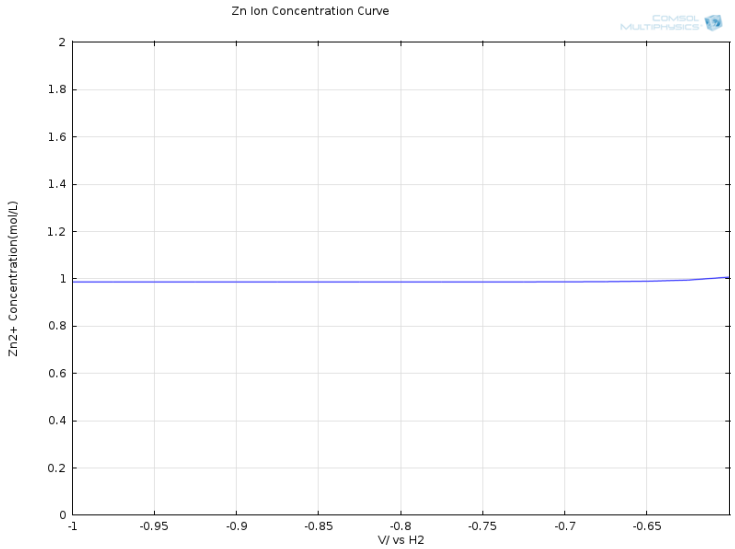

Figure 4.13: Zn^{2+} Concentration
Zn^{2+} is initialized as 1M.

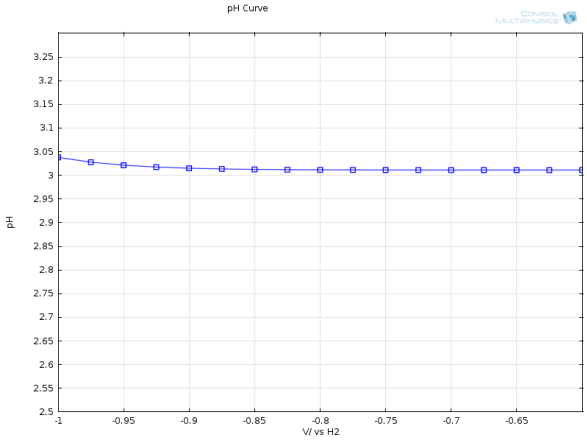

Figure 4.14: pH = 3
pH is initialized as 3.0.

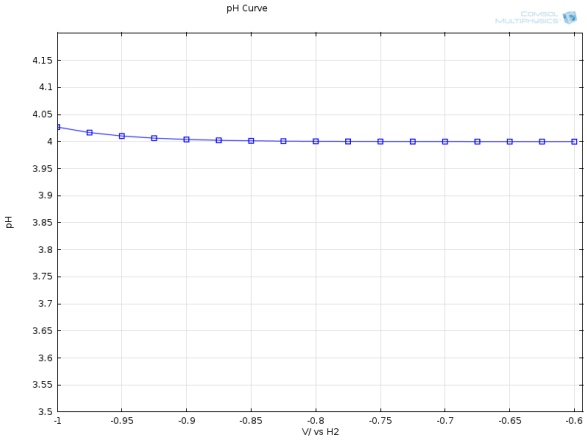

Figure 4.15: pH = 4
pH is initialized as 4.0.

reduction to H_2. The Tafel curves at two H^+ are shown in Figure 4.16 and Figure 4.17.

Both corrosion potential at pH=3.0 and pH=4.0 are around -0.74V to -0.76V, which are similar compared with the experimental result. (Experimental measurement of cor-

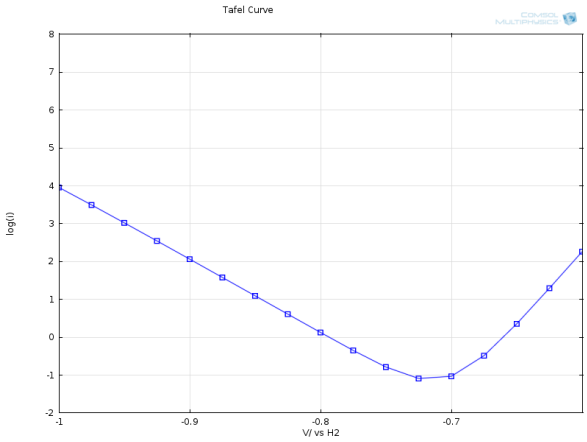

Figure 4.16: Tafel I pH3.0

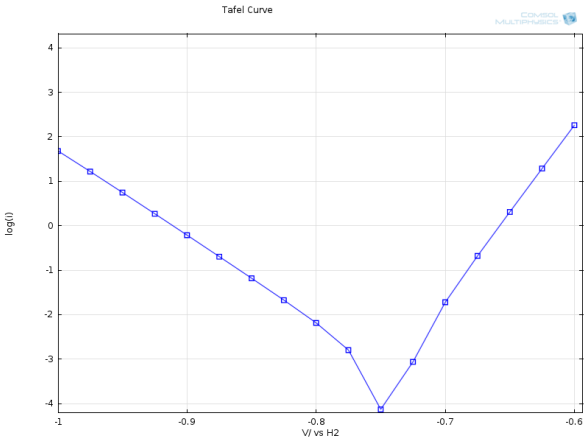

Figure 4.17: Tafel II pH4.0

rosion potential -1.44V relative to $Hg/HgSO_4$, is converted to -0.788V relative to SHE.) But pH=3.0 situation has a slightly higher corrosion potential compared with pH=4.0 situation based on the simulation. The equilibrium potential of hydrogen reaction can help explain this phenomenon. Because the hydrogen concentration polarization part (which is $\frac{2.3RT}{nF} \log \frac{(H^+)^2}{p_{H_2}}$) depends on the hydrogen ion concentration. The higher the concentration of H^+, the larger the polarization (or smaller the absolute value of polarization, since the polarization here is negative). Therefore pH=3.0 equilibrium potential is higher than pH=4.0 equilibrium potential in terms of H_2 reaction. This causes pH=3.0 final corrosion potential slightly larger.

4.2.4 Conclusion

In summary, the model was successful in simulating the linear polarization phenomenon on Zn surface when in contact with electrolyte. Compared with experimental results, the model derives the logarithmic corrosion current values of around -1 and -4 at the corrosion potential of around -0.72V and -0.75V(versus SHE), which are at the same magnitudes with experimental data of -3 from the logarithmic corrosion current and -1.43V(versus $Hg/HgSO_4$)corrosion potential. Meanwhile the model's corrosion potential results are also consistent with theoretical principle of concentration polarization influence.

Chapter 5

Atomistic Models

5.1 Introduction

The feature of electrochemical deposition is that the onset potential ($U(M^{n+}/S)$) is more negative than the equilibrium potential of the metal ion ($U_{eq}(M^{n+}/M)$), which gives rise to the so-called overpotential $\eta(M^{n+}/S) = |U(M^{n+}/S) - U_{eq}(M^{n+}/M)|$ [72]. Two directions of growth can potentially happen during electrochemical deposition. They are vertical and lateral growth.

In terms of a system, the onset potential $U(M^{n+}/S)$ is very close to the equilibrium potential $U_{eq}(M^{n+}/M)$, the calculated overpotential is thus comparably small. In the experiment, it is observed that the attachment of metal ions on the substrate is slow, and the growth is usually described as layer-by-layer (or spiral) growth. Under this condition, electrochemical deposition is considered to be governed by kinetic control, and dendrites do not significantly form. As the potential becomes more negative, the flux to the island on the substrate increases, and the layer-by-layer growth can not be sustained on the surface. In other words, the deposition transits from the kinetic control to the diffusion control with the increase of overpotential. When the overpotential is quite large, the nucleation becomes very fast and growth instabilities can lead to the formation of unusual dendrite morphologies. Figure 5.1 below illustrates the surface profile in a potential range [73].

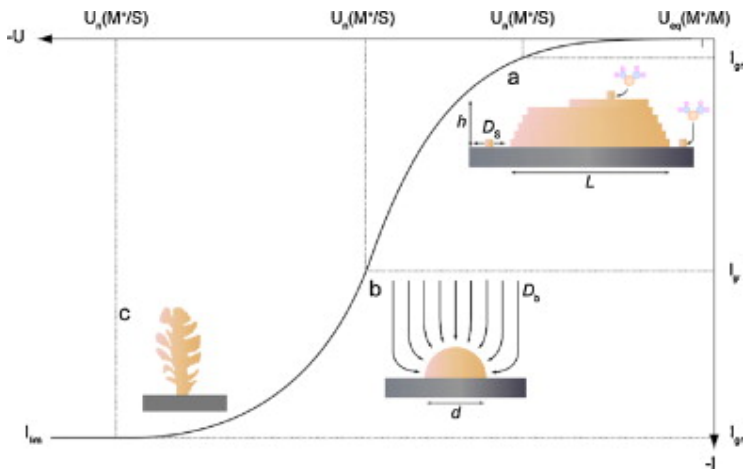

Figure 5.1: Potential Vs Electrochemical-deposition
There are two main regions combined with a mixed region in the graph. Region (a) is kinetic control; region (b) is mixed kinetic-diffusion control; region (c) is diffusion control. Region (a) is governed by layer-by-layer growth; region (b) is a transition region where dendrite starts to form; region (c) has diffusion limited aggregation or dendrite formation.

This section of atomistic simulation is operated in the diffusion-controlled region. Two parts are covered with respect to overpotential influence. The first part simulates the dendrite formation at different overpotential; the second part simulates the remaining ion distribution at the metal surface at different overpotential.

5.2 Diffusion-limited Dendrite Formation

The diffusion-limited aggregation provides a basis for modeling dendrite growth in the diffusion-controlled region [74]. During the process, dendrite are grown from a line electrode by electrodeposition under the diffusion-limited condition. The diffusion-limited condition is described by metal ions moving in a random manner and finally being deposited to a growing structure. Simulation can help obtain the growth patterns and average heights grown at different overpotential.

5.2.1 Random Walk

Random walk process is usually used in the diffusion-limited growth. It is defined as the current value of a variable composed of the past value plus an error term defined as a white noise (statistically zero mean and variance one). The mathematical expression is

$$y_t = y_{t-1} + \epsilon_{t-1} \tag{5.1}$$

The implication of the process is that the prediction for the change $(y_t - y_{t-1})$ is not allowed, meaning the change of y is random. But the average value of a random walk process is a constant even though the variance changes at each step. In the simulation, the metallic ion undergoes random walk until it is ultimately fixed at a position.

5.2.2 Simulation Methods

Monte Carlo simulation method has been proved to be a simple but efficient approach in numerical computation. It is one of the most widely used stochastic methods. In the diffusion-limited aggregation simulation, this probability theory is implemented to decide an atom deposition based on the sticking coefficient criteria.

In the study, each atom performs a random walk from the top to the bottom until it gets stuck on the substrate or metal surface. Their positions are randomly selected. During the flow, each atom has four possible neighbouring sites to choose if all the neighbouring sites are vacant. If one or more sites are occupied by another atom, the flowing atom has an opportunity to be deposited against that atom. It is assumed in the simulation that once the atom gets deposited on the surface, it becomes an immobile atom and one part of the growth site. The probability of deposition P_{stick}, also denoted as sticking coefficient [75], is expressed as

$$P_{stick} = \frac{f_c(\eta) - f_a(\eta)}{f_c(\eta) + f_a(\eta) + I_L/I_0} \tag{5.2}$$

where $f_c(\eta) = \exp(\frac{-\alpha_c F\eta}{RT})$ and $f_a(\eta) = \exp(\frac{\alpha_a F\eta}{RT})$; η is known as overpotential; F is the Faraday constant; α_a and α_c are anodic and cathodic coefficient separately; I_0 is the exchange current and I_L is the limiting current [76]. The cathodic term is given a minus

sign by convention when the overpotential η is used as a true negative value rather than an absolute value.

The decision of whether an atom sticks to the surface or not depends on comparing the sticking coefficient P_{stick} with a random number P_{rand}. If P_{rand} is less than P_{stick}, the atom will be successfully deposited; otherwise it will continue flowing. The boundary condition in this simulation is defined such that, if an atom goes outside the study domain in its random flowing, it will re-enter the domain from the other side. Each cycle of simulation focuses only on one atom, meaning when one atom is fixed as immobile, the next atom gets started by flowing from the top to the bottom. Therefore in the simulation, the number of atoms is predefined. When all the atoms are deposited, the whole simulation ends. However, if one atom has equal probability of going to four directions and starts from the top, it will take a long time until it finally gets to the bottom. Thus, in order to speed up the simulation, atoms are defined with a probability of 0.375 flowing down, a probability of 0.125 flowing up, and a probability of 0.25 flowing left and right. (It is assumed that atoms have equal probabilities of flowing to the left or to the right, but higher probabilities of flowing downside than upside. This is only for the sake of computation.) In the simulation, 3000 flowing atoms are used for deposition with different overpotential. The simulation cares both two dimensional case and three dimensional case in the following discussions.

5.2.3 Results and Discussion

The equilibrium potential for zinc is -0.763V with respect to the standard hydrogen potential. The simulation assumes that I_L/I_0 is universally defined as 1. The temperature used is room temperature 300 K. anodic and cathodic coefficient based on the literature are both set as 0.5 ($\alpha_a = \alpha_c = 0.5$). Figure 5.2 below shows the sticking coefficient with different overpotential. For all the graphs, the overpotential η is changed to be an absolute value ($|\eta|$).

The following several graphs from Figure 5.3 to Figure 5.8 show the dendrite morphologies at different overpotentials of 0.01V, 0.04V, 0.08V, 0.12V, 0.15V and 0.30V in the two dimensional simulation. In all these graphs, y-axis represents the number of atoms

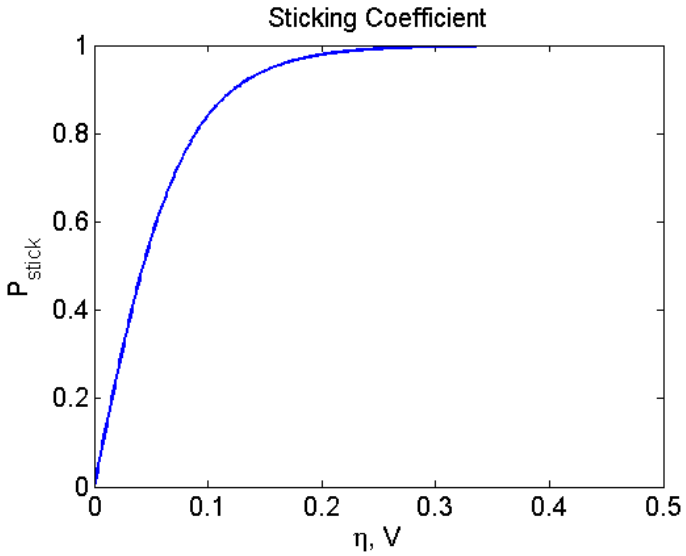

Figure 5.2: Sticking Coefficient Vs Overpotential
The sticking coefficient plot with respect to overpotential η based on the calculation.

deposited on the surface, which illustrates the height of the dendrites. x-axis represents the domain defined in the simulation with the same magnitude as the atom size.

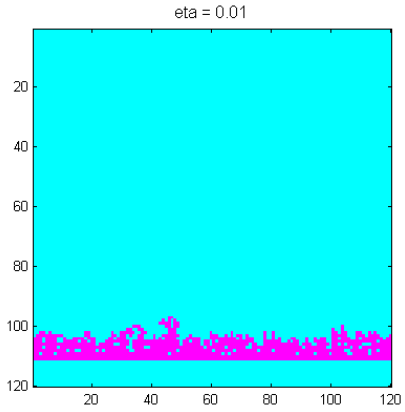

Figure 5.3: Dendrite Formation $|\eta| = 0.01V$

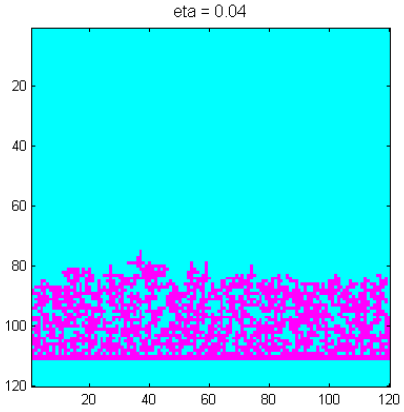

Figure 5.4: Dendrite Formation $|\eta| = 0.04V$

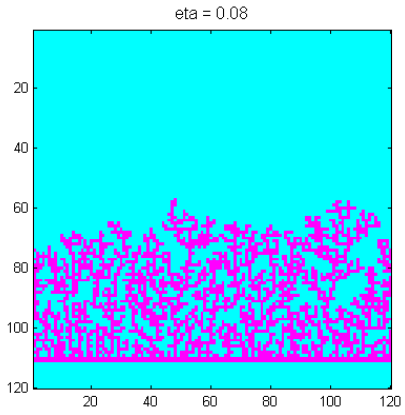

Figure 5.5: Dendrite Formation $|\eta| = 0.08V$

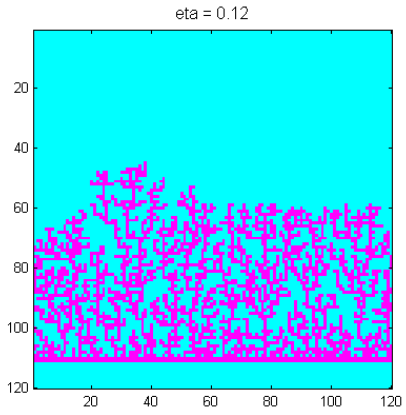

Figure 5.6: Dendrite Formation $|\eta| = 0.12V$

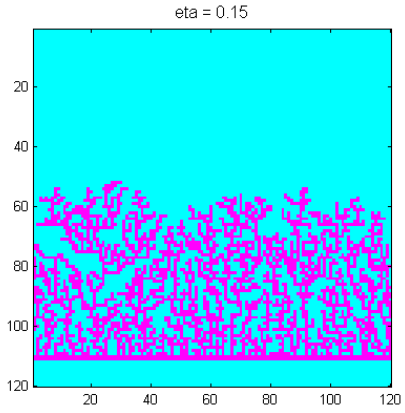

Figure 5.7: Dendrite Formation $|\eta| = 0.15V$

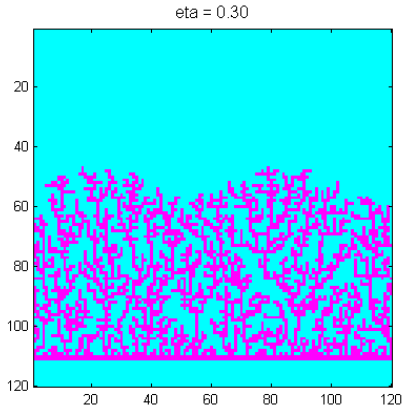

Figure 5.8: Dendrite Formation $|\eta| = 0.30V$

When $|\eta| = 0.01V$, the overpotential is too small to be controlled by diffusion in the real situation. But at the same time, results via diffusion-limited aggregation method still show that small overpotential causes lower height. The atoms are densely deposited with each other. When overpotential increases to 0.04V ($|\eta| = 0.04V$), the dendrite morphology is very clear to be observed. The space inserted inside the deposited film is bigger compared with the case from overpotential 0.01V. When overpotential increases to a larger value over 0.1V such as 0.12V or 0.15V, the dendrite height formed is also increasing. But in terms

of 0.30V overpotential, the height is not significantly higher than 0.15V or 0.12V. It can be confirmed by observing the sticking coefficient curve P_{stick} versus $|\eta|$, that P_{stick} quickly converges to 1 when $|\eta|$ is around 0.15V.

Three dimensional simulation further confirms the tendency of dendrite formation with different sticking coefficients. The graphs from Figure 5.11 to Figure 5.16 show the morphologies with directly calculated sticking coefficients.

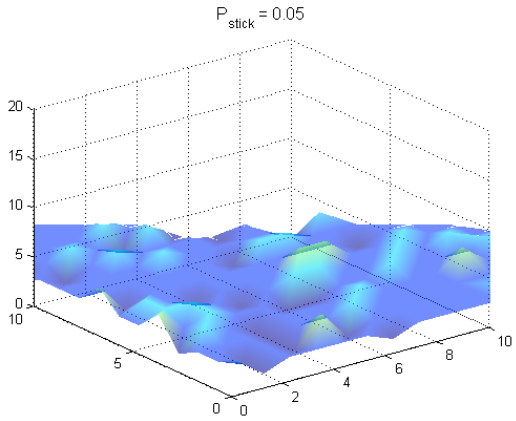

Figure 5.9: Dendrite Formation $P_{stick} = 0.05$

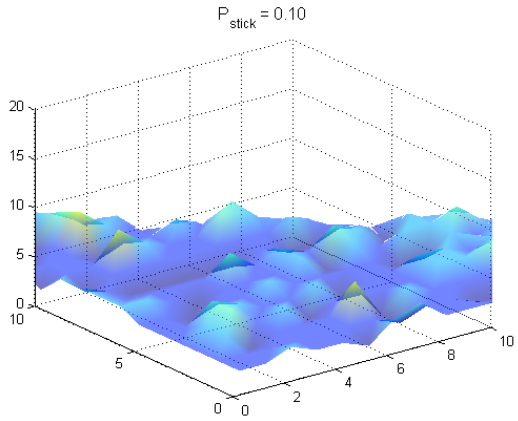

Figure 5.10: Dendrite Formation $P_{stick} = 0.10$

The table 5.1 records the simulation data listing overpotential (η), sticking coefficient (P_{stick}) and growth height (n_{atom}). Even though only 3000 particles are used in the simulation, the result still shows the tendency of the relationship between overpotential and growth height at the diffusion-limited region.

From the statistical point of view, the above simulations study the dendrite heights at different overpotential based on a governing sticking coefficient P_{stick} formula. In the experiment, it is observed that at the diffusion-limited region, the larger values of overpotential usually cause higher dendrites and varied island orientations [73]. The simulation in this study confirms the results by incorporating a proved formula using diffusion-limited aggregation method.

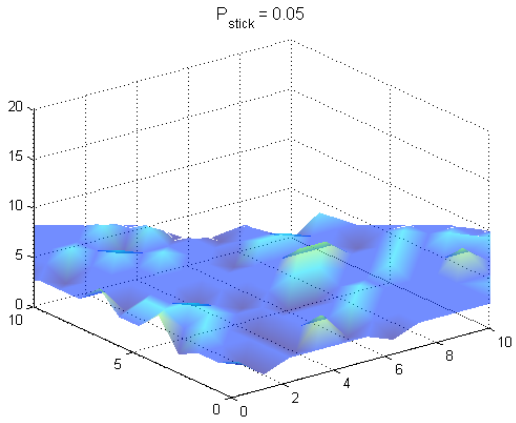

Figure 5.11: Dendrite Formation $P_{stick} = 0.05$

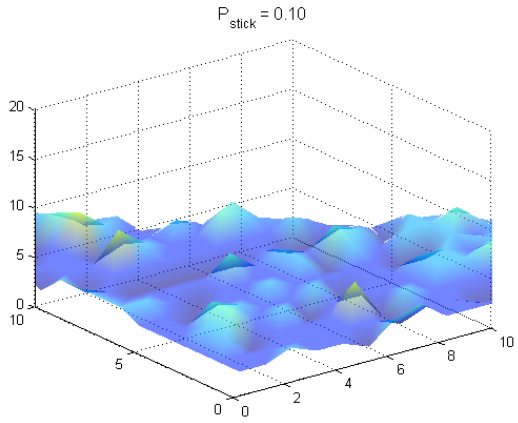

Figure 5.12: Dendrite Formation $P_{stick} = 0.10$

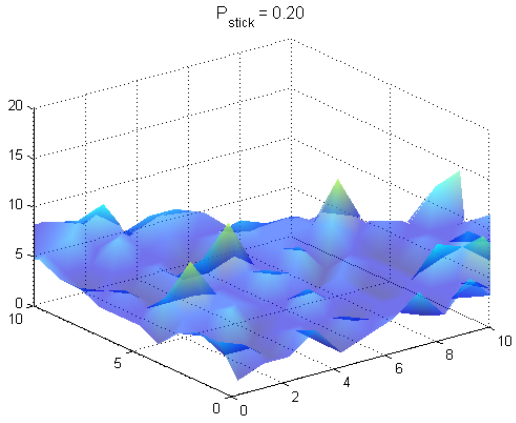

Figure 5.13: Dendrite Formation $P_{stick} = 0.20$

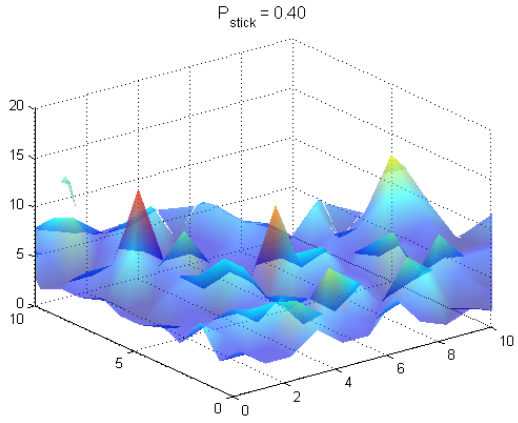

Figure 5.14: Dendrite Formation $P_{stick} = 0.40$

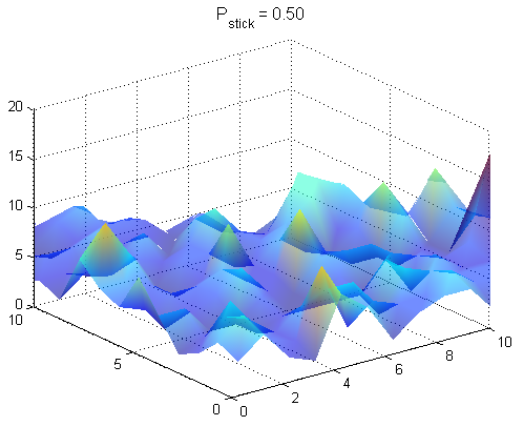

Figure 5.15: Dendrite Formation $P_{stick} = 0.50$

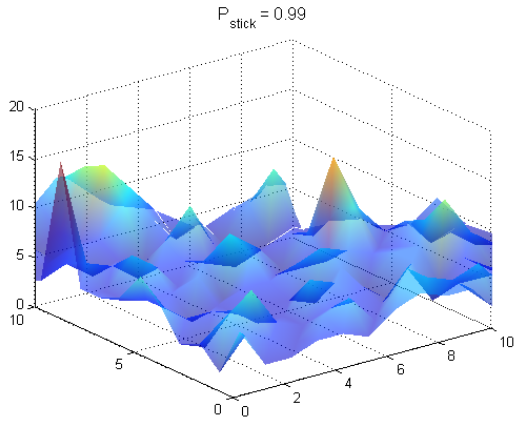

Figure 5.16: Dendrite Formation $P_{stick} = 0.99$

Overpotential (η)	Sticking Coefficient (P_{stick})	Height (n_{atom})
-0.01	0.1282	13
-0.02	0.2518	22
-0.04	0.4705	35
-0.08	0.7591	53
-0.10	0.8403	58
-0.12	0.8941	65
-0.15	0.9425	59
-0.20	0.9787	69
-0.25	0.9920	68
-0.30	0.9975	65

Table 5.1: Dendrite Growth Height

The data in the table shows that generally with increment of overpotential η absolute values, sticking coefficients P_{stick} increase, accompanied by the increase of the dendrite heights.

5.3 Metallic Ion Distribution

In this session of study, the focus switches from the metallic atoms deposited on the surface to the metallic ions left inside the solution. It is in fact a parallelled investigation from another angle, while a different simulation method is implemented. Stochastic diffusion-reaction process, in another name kinetic Monte Carlo method is presented and applied in the study. The electrochemical deposition-dissolution process is executed by stochastic reaction. Metallic ions diffusing at the surface is executed by stochastic diffusion. The subsequent sections will introduce stochastic reaction, diffusion and the combined process separately. Finally the combined method will entirely simulate the assumed situation of electrochemical deposition.

5.3.1 Stochastic Reaction

For a general chemical reaction such as,

$$M \xrightarrow{k} \phi \tag{5.3}$$

in which M is the reaction species and k is the rate constant of the reaction. Here we are mainly concerned about species M, while species ϕ is considered as a species with no interests. The rate constant k is given here so that the term kdt is defined as the probability of any atom randomly chosen. dt is denoted as the time interval between $[t, t+dt)$. Usually the number of atoms change over time, so $M(t)$ means the number of atoms at the specific time t. Given all the necessary concepts, the probability that an atom gets reacted during the time interval $[t, t+dt)$ is calculated as $M(t)kdt$ [77].

In the simulation, this probability is compared with a random number P_{rand} uniformly generated in the region $(0, 1)$. If the number $M(t)kdt$ is bigger than P_{rand}, the event is accepted, giving rise to the atomic number reduction [49].

From the definition, if the time interval dt is defined too large, or the reaction rate k is too high, or the atomic number is very big, the reaction probability $M(t)kdt$ can go high enough beyond 1. In this case, during every time interval dt, the atomic number always

decreases. However, when the number becomes small, the product of $M(t)kdt$ becomes small too. Thus the probability can result in $M(t)kdt < P_{rand}$, when there is no reaction during this interval. By experimental observation, the reaction rate cannot always keep high, and ultimately it will be stabilized at a certain value or even decrease to 0.

It is also very likely that the product of $M(t)kdt$ is much less than 1. Therefore, the simulation needs a big trial cycling number until at one time $M(t)kdt > P_{rand}$. A speedup technique in the stochastic simulation is usually used to substitute the conventional method. The speedup algorithm alternatively calculates a time step, named τ, after which one reaction definitely happens [78]. Hence from the assumption, the reaction happening probability after time period τ is

$$P = \exp[-M(t)k\tau] \tag{5.4}$$

After the minimum time period, a newly generated random number P_{rand} should be equal to the probability shown above.

$$\tau = \frac{1}{M(t)k} \ln[\frac{1}{P_{rand}}] \tag{5.5}$$

Therefore, a general stochastic reaction algorithm is organized as follows.

Algorithm 1 Stochastic Reaction

Require: Reaction rate k_{rec};

1. Generate one random number r;

2. Compute the time τ with r when next reaction occurs at $t + \tau$;

3. Compute the number of atoms at $t + \tau$ by $M(t + \tau) = M(t) - 1$;

4. Go back to Step **1** at $t + \tau$;

This algorithm can be used for both atom deposition and dissolution problem in the study. The requirement should be changed to deposition rate k_{dep} and dissolution rate k_{dis}. Meanwhile, since the events are happening in the diffusion-controlled region, sticking coefficient P_{stick} should be further multiplied with the deposition rate k_{dep}.

5.3.2 Stochastic Diffusion

The surface atomic diffusion simulation can adopt a similar approach as introduced in the reaction case, but the stochastic selection needs to separate atoms into different compartments [79]. In terms of a one dimensional simulation, the domain with a length L can be averagely divided into K compartments. Thus, each atom is allocated into one compartment. One compartment can have zero, one or more than one atoms. The length of each compartment is defined as $h = L/K$. For ith compartment ranging from $[(i-1)h, ih)$, the number of atoms inside is $M_i(t)$. Therefore diffusion stochastic form is

$$M_1(t) \overset{d}{\rightleftharpoons} M_2(t) \overset{d}{\rightleftharpoons} \ldots \overset{d}{\rightleftharpoons} M_k(t) \tag{5.6}$$

$M_i(t) \overset{d}{\rightleftharpoons} M_{i+1}(t)$, interpreted as $M_i(t) \overset{d}{\rightarrow} M_{i+1}(t)$ and $M_i(t) \overset{d}{\leftarrow} M_{i+1}(t)$, means one atom with the rate d diffuses to the right side or left side. The rate constant d is calculated as $d = D/h^2$, in which D is the conventional diffusion coefficient and h is the compartment length [80].

During simulation, the diffusion propensity function is expressed as $\alpha_i(t) = M_i(t)d$, where $i = 1, 2, \ldots, K$. And the whole propensity function is the sum of diffusion going to the left and going to the right.

$$\alpha_{sum}(t) = \sum_{i=1}^{K-1} \alpha_i(t) + \sum_{i=2}^{K} \alpha_i(t) \tag{5.7}$$

Thus the stochastic diffusion algorithm is derived as follows.

The metallic ions diffusion can directly incorporate the above algorithm.

Algorithm 2 Stochastic Diffusion

Require: Diffusion coefficient D;

1. Generate two random numbers r_1, r_2;

2. Compute the propensity functions given as

$$\alpha_0 = \sum_{i=1}^{K-1} \alpha_i + \sum_{i=2}^{K} \alpha_i \tag{5.8}$$

where $\alpha_i = M_i(t)d$, $d = D/h^2$;

3. Compute time τ with r_1 when next diffusion occurs at $t + \tau$;

4. Choose the direction of diffusion;

if $r_2 < \sum_{i=1}^{K-1} \alpha_i/\alpha_0$ **then**

Find $j \in 1, 2, \ldots, K-1$;

Such that $r_2 \geq \frac{1}{\alpha_0} \sum_{i=1}^{j-1} \alpha_i$ and $r_2 \leq \frac{1}{\alpha_0} \sum_{i=1}^{j} \alpha_i$;

DO $M_j(t+\tau) = M_j(t) - 1$ and $M_{j+1}(t+\tau) = M_{j+1}(t) + 1$;

else

Find $j \in 2, 3, \ldots, K$;

Such that $r_2 \geq \frac{1}{\alpha_0}(\sum_{i=1}^{K-1} \alpha_i + \sum_{i=2}^{j-1} \alpha_i)$ and $r_2 \leq \frac{1}{\alpha_0}(\sum_{i=1}^{K-1} \alpha_i + \sum_{i=2}^{j} \alpha_i)$;

DO $M_j(t+\tau) = M_j(t) - 1$ and $M_{j-1}(t+\tau) = M_{j-1}(t) + 1$;

end if

4. Go back to Step **1** at $t + \tau$;

5.3.3 Stochastic Diffusion-Deposition-Dissolution

Eventually, deposition, dissolution and diffusion are combined together for the entire electrochemical deposition simulation. Zinc ions are assumed to be the metallic ions.

$$M_{Zn^{2+}}(t) \longrightarrow \phi \qquad \text{Deposition} \tag{5.9}$$

$$\phi \longrightarrow M_{Zn^{2+}}(t) \qquad \text{Dissolution} \tag{5.10}$$

$$M_{Zn^{2+},1}(t) \overset{d}{\leftrightharpoons} M_{Zn^{2+},2}(t) \overset{d}{\leftrightharpoons} \ldots \overset{d}{\leftrightharpoons} M_{Zn^{2+},k}(t) \qquad \text{Diffusion} \tag{5.11}$$

The specific parameters for Zn^{2+} diffusion coefficient, deposition or dissolution are pretty vague. It largely depends on the external environment. However this study mainly aims to prove the overpotential influence on the number of metallic atoms on the surface. It can also be extended to other metallic ions. Due to an additional sticking coefficient on the deposition, the true propensity function of deposition in the simulation is $P_{stick}M(t)k_{dep}$.

The final diffusion-deposition-dissolution algorithm is shown below.

Algorithm 3 Stochastic Diffusion-Deposition

Require: Diffusion coefficient D;
Require: Deposition rate k_{dep};
Require: Dissolution rate k_{dis};
Require: Sticking coefficient P_{stick};

1. Generate two random numbers r_1, r_2;
2. Compute the propensity functions in two parts
$A_i(t)d$ for diffusion and $M_i(t)k_{dep}P_{stick}$ for deposition;
3. Decide deposition or diffusion similar to **Stochastic Diffusion**;
4. Go back to Step **1** at $t + \tau$;

5.3.4 Results and Discussion

There is not enough information about the exact diffusion coefficient and deposition rate of Zn^{2+} and dissolution rate of Zn atoms in the aqueous environment. In the sophisticat-

ed lattice atomic calculation, some formulas are proposed to describe molecular rate for dissolution, deposition and diffusion. [81]

However these calculations are based on pure metal deposition on substrate at certain environment, which are quite different from the metallic ions deposited on the metal surface in the aqueous environment. Therefore, this study simply uses some general and fixed rate parameters to simulate the remaining number of ions in the solution via stochastic method.

From most literatures, the diffusion coefficient of ions in the solution ranges from 10^{-9} to 10^{-7} $[cm^2/s]$. In order to accelerate the simulation, the study here chooses $10^{-7}[cm^2/s]$ for diffusion coefficient D. In terms of deposition and dissolution rate representing $Zn^{2+} \rightarrow Zn$ and $Zn \rightarrow Zn^{2+}$, many research groups have reported that the surface diffusion events have way higher rate than deposition, which results in a very long time until one monolayer is successfully deposited [54, 57]. Regarding the time spent in the simulation and also balancing the influence from diffusion process, the study picks two reaction rates, namely deposition and dissolution rate to be $1.2 \cdot 10^{-3}[s^{-1}]$ and $1.5 \cdot 10^{-3}[s^{-1}]$.

The domain is separated into five regions with five sticking coefficients for deposition. The first part of simulation has the sticking coefficient distribution as [0.7 0.3 0.1 0.9 0.5]. The simulations use different time periods (5min, 10min, 20min, 40min) to test the remaining metal ions on the surface.

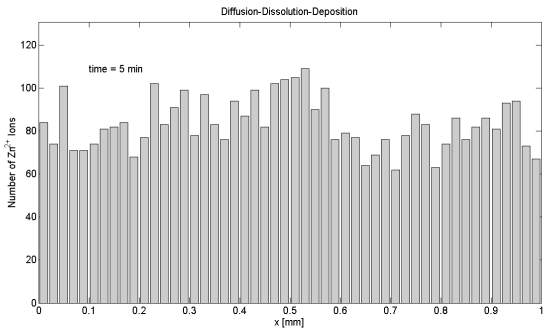

Figure 5.17: 5.0 min Simulation

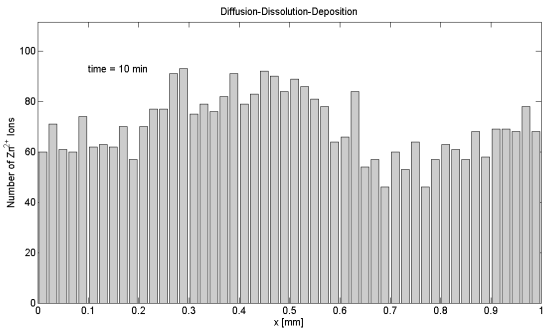

Figure 5.18: 10 min Simulation

x-axis is the domain of simulation from 0 to 1, and y-axis the number of ions left after 5 and 10 minutes.

In Figure 5.17 when time period is 5 minutes, the ions are almost averagely distributed inside the whole domain. Meanwhile the region with the highest number of ions still have

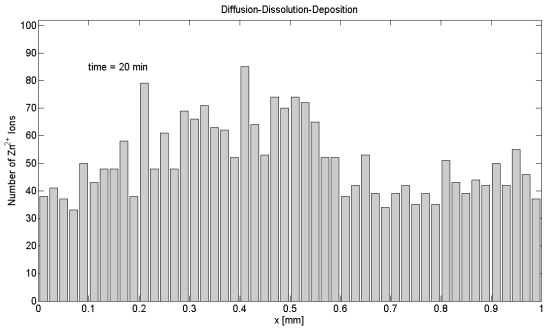

Figure 5.19: 20 min Simulation

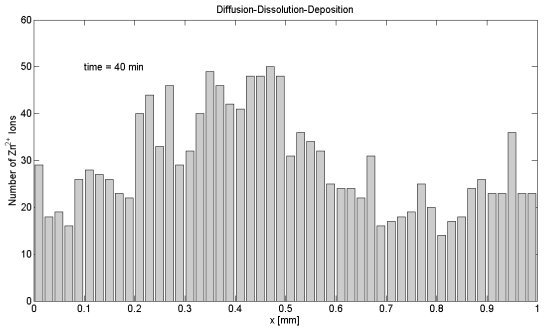

Figure 5.20: 40 min Simulation

x-axis is the domain of simulation from 0 to 1, and y-axis the number of ions left after 20 and 40 minutes.

number around 100. It is due to the fact that diffusion rate is higher than the other two rates, which causes small changes on the ion number. When the period gets longer, more ions are deposited on the surface. And the sticking coefficient factor gradually influences the distribution of ions on the surface, such as in Figure 5.19 and Figure 5.20. It can be seen that the middle part of domain gets more ions while the two end sides maintain smaller number of ions. Because in the middle region, sticking coefficient is set as 0.1, this small probability will reject many trials of deposition. In comparison higher sticking coefficients such as 0.9 on the right and 0.7 on the left give rise to higher probability of deposition.

In the next study, regions with different sticking coefficient distributions are simulated via stochastic method. Different sticking coefficients simulate the conditions when the over-potentials at the substrate or metal surface are distributed unevenly, and the results can illustrate some of the potential influence on the remaining ion distribution after long simulation time. The time period for all the following conditions is set the same as 30min. The simulations consider three different situations: [0.7 0.3 0.1 0.9 0.5], [0.1 0.3 0.5 0.7 0.9] and [0.9 0.7 0.5 0.3 0.1].

The three figures from Figure 5.21, Figure 5.22 and Figure 5.23 distinctively illustrate the sticking coefficient influence on the final ion distribution. When the sticking coefficient is large, it is more likely that the ions can be deposited on every deposition trial, which shows less ions left in this region. In contrast, the low sticking coefficient area can reject

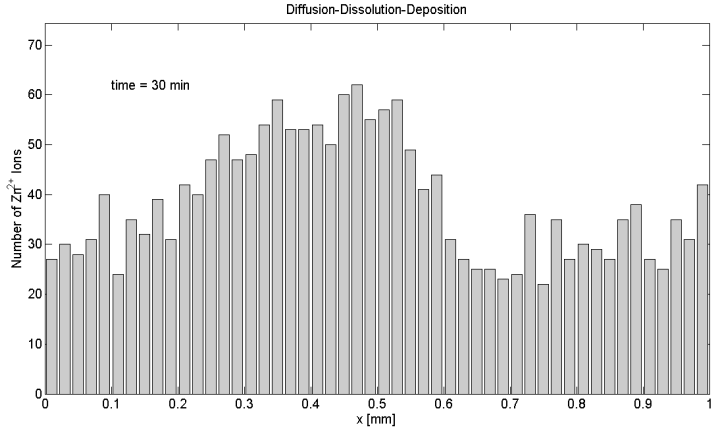

Figure 5.21: Sticking Coefficient Distribution: [0.7 0.3 0.1 0.9 0.5]

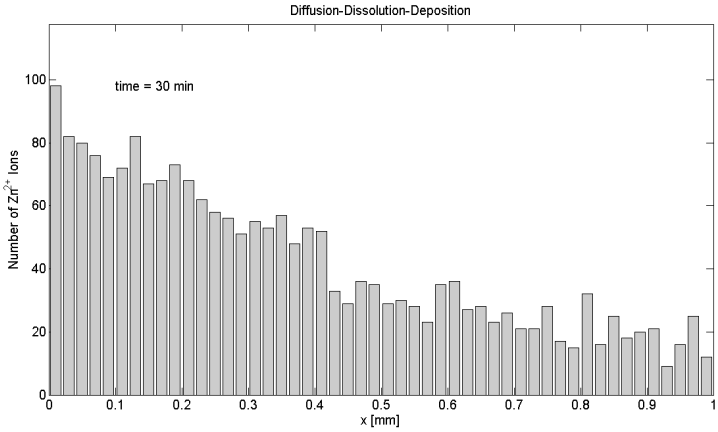

Figure 5.22: Sticking Coefficient Distribution: [0.1 0.3 0.5 0.7 0.9]

more deposition trials, thus showing more ions left on the surface.

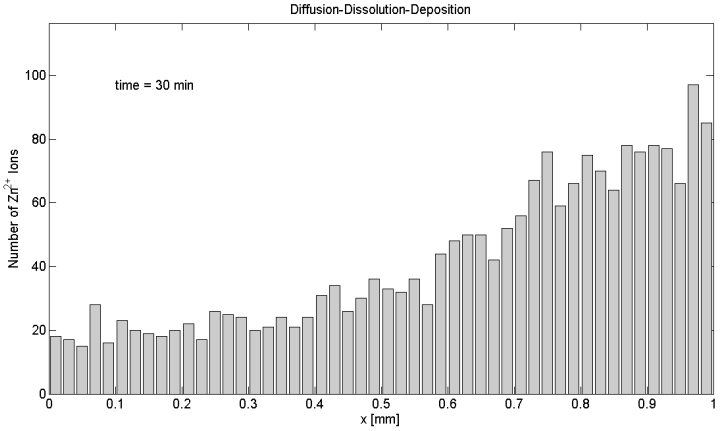

Figure 5.23: Sticking Coefficient Distribution: [0.9 0.7 0.5 0.3 0.1]

5.4 Conclusion

Dendrite formation and metal ion consumption are simulated via atomistic model. The model is constructed stochastically assisted with a sticking coefficient theory. Both simulated results show that overpotential has a big influence at the diffusion-controlled region. Higher overpotential can accelerate the dendrite growth; also in the meantime decreases the number of ions in that region if operated in a long time. The results may guide experimental tests and designs if better Zn morphology is expected.

Chapter 6

Conclusions

6.1 Conclusions

A series of modeling strategies covering empirical, electrochemical engineering, and atomistic level have been implemented on the ReHAB system. At the empirical level, particle filter method is executed on the raw battery data from experiments to track and predict battery capacity at higher numbers of cycles. At the electrochemical engineering level, in terms of cathode $LiMn_2O_4$, battery interface module and porous transport theory give a good illustration to simulate battery charge/discharge process. An additional side reaction exchange current density formula is added in the model to simulate the constant-current constant-voltage process. In terms of anode Zn, the simulation is focused on the corrosion. Nernst-Planck interface combining electrochemical reactions and chemical reactions is used to study thermodynamics during corrosion, by illustrating the Tafel curves at different pH values. At the atomistic level, the thesis studies the diffusion-controlled region where diffusion-limited aggregation technique is implemented. Via sticking coefficient and probability theory, it is found that higher overpotential can give rise to more severe dendrite growth, and more ions consumed in the long time. General conclusions of this thesis are listed as:

- The empirical relationship between Coulombic efficiency η_C and cycle capacity C_k is

valid in ReHAB cell.

- Particle filter method is proved to be an efficient method in tracking and predicting battery cell performance.
- Butler-Volmer interface kinetic of Li and anodic kinetic of Zn can be combined together in cell operation.
- A reaction current opposite to the charge or discharge current direction at the electrode can be used as a side reaction expression.
- Nernst-Planck interface can accurately model the corrosion potential and illustrate the hydrogen concentration polarization influence.
- At the diffusion-controlled region, the stochastic theory proves that higher overpotential can lead to rougher surface and faster ion deposition.

6.2 Recommendations

Since this is the first trial of simulating ReHAB system at different levels, more work with deeper depth can be done in the future study.

- Empirical level:
  - The nonlinear term obtained from η_C calculating capacity and measured capacity deserves deeper study. The empirical model can be derived back to cell circuit model, whose parameters are linked with cell material properties. Particle filter achieves the tracking convergence via the convergence properties from numbers of sampled particles, but the nonlinear terms are covered inside the Gaussian noise assumption. It is worthwhile designing a better algorithm focusing on the nonlinear terms with respect to different battery materials.
- Electrochemical engineering level:

  - The conventional pseudo 2D model is used in this part to simulate cathode. The original pseudo 2D model is designed for organic electrolyte but ReHAB has aqueous electrolyte solution. Therefore it requires a more sophisticated study on the model design with more emphasis on H_2O influence.
  - The added side reaction current density is only a simple assumption, while more work could be done to make a more accurate expression for side reaction during charge/discharge, since the charge process in the simulation is not consistent with the experiments. Also there can be other possibilities causing side reactions except for an additional current term.
  - The potential chemical reactions in the model are only assumed without further study. Meanwhile anode corrosion does not consider cathode influence and cathode Li intercalation does not incorporate anode corrosion effects. Thus a better model on the how anode affects cathode performance or how cathode affects anode performance is needed to understand the interconnected side effects.

- Atomistic level:
  - The study only cares about one aspect of overpotential on Zn dendrite formation in the diffusion-controlled region, but a more sophisticated study usually incorporates atomic energy calculation at step of calculation. An extended simulation on the lattice structure with Zn atom energy at different state computation should be considered in the future.

Appendix

Matlab Code in Simulation

Particle Filter Code

The key parts of the particle filter Matlab code are put here.

Load battery performance data from C hard drive.

```
file_coin_SFG = 'C:\Users\Han\140326\SFG-6\A3.xls';
data_coin_SFG = xlsread(file_coin_SFG);
% file_coin_KS = 'C:\Users\Han\140326\KS-15\C3.xls';
% data_coin_KS = xlsread(file_coin_KS);
% file_swig_SFG = 'C:\Users\Han\140326 swig log\SFG-6\B3.xls';
% data_swig_SFG = xlsread(file_swig_SFG);
% file_swig_KS = 'C:\Users\Han\140326 swig log\KS-15\D3.xls';
% data_swig_KS = xlsread(file_swig_KS);

efficiency = data_coin_SFG(20:800,6);
capacity = data_coin_SFG(20:800,3);
```

Compare Coulombic efficiency calculation with true measurement data.

```
x_CE = zeros(length(capacity),1);
```

```
x_CE(1) = capacity(1);
for i = 1 : length(capacity)-1
    x_CE(i+1) = x_CE(i)*efficiency(i)/100;
end

x_Left = capacity(:) - x_CE(:);

figure;
T = length(capacity);
t = 1 : T;
plot(t,capacity,'.-b',t,x_CE,'.-g',t,x_Left,'.-r','linewidth',3)
legend('True capacity', 'Modeled capacity', 'Non-linear part capacity')
xlabel('Cycles')
ylabel('Capacity')
fprintf('CE, xLeft = %f\n', abs(x_Left(500)))
```

Particle filter method tracking and prediction.

```
x = capacity(1);
N = 100;    % Particle number
x_N = 0.0025;
x_R = 0.001;
T = length(capacity);

V = 2;      % Initial variance estimate
x_P = [];
for i = 1 : N
    x_P(i) = x + sqrt(V)*randn;
end
for t = 2 : T
    for i = 1 : N
        % Update process
```

```
        x_P_update(i) = efficiency(t-1)/100*x_P(i) + x_N*randn;
        % Weight every particle
        P_w(i) = 1/sqrt(2*pi*x_R) * exp(-(capacity(t)-x_P_update(i))^2/(2*x_R));
    end
    % Normalize the weight
    P_w = P_w./sum(P_w);
    % Resample
    for i = 1 : N
% Use cumulative command to randomly choose the
        % first element satisfying (>= rand)
% The more probable, the more likely to be chosen, which is KMC idea
        x_P(i) = x_P_update(find(rand <= cumsum(P_w),1));
    end
    % Get the particle estimate for current cycle
    x_est = mean(x_P);
    % Load the estimate for the whole process
    x_est_out = [x_est_out x_est];
end
% ========================================================================
% Particle filtering of the estimated efficiency
eff = 99.8847;
capacity_new = capacity(T1);
x_R = 1;

for t = T1+1 : T
    for i = 1 : N
        % Update process
        x_P_update(i) = eff/100*x_P(i) + x_N*randn;
        % Weight every particle
capacity_new = capacity_new*eff/100;
        P_w(i) = 1/sqrt(2*pi*x_R) *
```

```
        exp(-(capacity_new-x_P_update(i))^2/(2*x_R));
    end
    % Normalize the weight
    P_w = P_w./sum(P_w);
    % Resample
    for i = 1 : N
% Use cumulative command to randomly choose the first
        % element satisfying (>= rand)
% The more probable, the more likely to be chosen, which is KMC idea
        x_P(i) = x_P_update(find(rand <= cumsum(P_w),1));
    end
    % Get the particle estimate for current cycle
    x_est = mean(x_P);
    % Load the estimate for the whole process
    x_est_out = [x_est_out x_est];
end



t = T1+1 : T;
plot(t,x_est_out(T1+1:T),'.-k',t,capacity(T1+1:T),'.-b','linewidth',3);
hold off
xlabel('Cycles'); ylabel('Capacity');
legend('True measurement','PF estimate with true CE',
 'PF estimate with estimated CE');

% ================================================
% Calculate the percentage difference
% ================================================
fprintf('myEst, xLeft = %f\n', abs(capacity(500)-x_est_out(500)))
fprintf('Est CE = %f\n', eff)
```

Dendrite Formation Code

Main Matlab code for dendrite formation and stochastic simulation code are listed here.

Sticking coefficient calculation.

```
alpha_c = 0.5;
alpha_a = 0.5;
F = 9.65e4;
R = 8.31;
T = 300;
eta = 0:-0.001:-0.5;
eta = eta';
fc = zeros(length(eta),1);
fa = zeros(length(eta),1);
Pstick = zeros(length(eta),1);
% Assume I/I_l = 1

for i = 1 : length(eta)
    fc(i) = exp(-alpha_c*F*eta(i)/(R*T));
    fa(i) = exp(alpha_a*F*eta(i)/(R*T));
    Pstick(i) = (fc(i) - fa(i)) / (fc(i) + fa(i) + 1);
end

figure
set(gca, 'FontSize', 15)
plot(eta,Pstick,'LineWidth',2)
title('Sticking Coefficient')
xlabel('\eta, V')
ylabel('P_{stick}')
```

Dendrite formation with sticking coefficient influence.

```
clear, clc, close all

% Start timing
tic

nParticles = 20000;
maxX = 10;
maxY = 10;
maxZ = 120;
zStart = 5;

nNewParticlesPerFrame = 10;

dX = 0.1;
dY = 0.1;
xx = dX:dX:maxX;
yy = dY:dY:maxY;
[X,Y] = meshgrid(xx,yy);
Z = zeros(length(xx));

PstickList = 0.99;
Height = 0;

f = zeros(length(PstickList),1);
rng('shuffle')

for j = 1 : length(PstickList)
    Pstick = PstickList(j);
    figure
    Z = zeros(length(xx));
    for i = 1 : nParticles
```

```
% x, y used for recording numbers, NOT Coordinate !!!!!
x = ceil(rand()*length(xx));
y = ceil(rand()*length(yy));
z = maxZ - zStart;

while 1
    xOld = x;
    yOld = y;
    zOld = z;
    rval = rand();
    % 5 Possiblities: [Down, North, South, West, East]
    if rval <= 0.5
        z = z - 1;
    elseif rval <= 5/8 && rval > 1/2
        x = x + 1;
    elseif rval <= 6/8 && rval > 5/8
        x = x - 1;
    elseif rval <= 7/8 && rval > 6/8
        y = y + 1;
    else
        y = y - 1;
    end
    if z < 0
        Z(xOld,yOld) = 1;
        break;
    end
    % Periodic boundary condition
    if x > length(xx)
        x = 1;
    end
    if x < 1
```

```
            x = length(xx);
        end
        if y > length(yy)
            y = 1;
        end
        if y < 1
            y = length(yy);
        end
%         if Z(x,y) == z
%             x = xOld;
%             y = yOld;
%             z = zOld;
%             continue;
%         end
        xR = mod(x,length(xx)) + 1;
        xL = mod(x,length(xx)) - 1;
        yR = mod(y,length(yy)) + 1;
        yL = mod(y,length(yy)) - 1;
        zU = z + 1;
        zD = z - 1;

        if xL < 1
            xL = length(xx);
        end
        if xR > length(xx)
            xR = 1;
        end
        if yL < 1
            yL = length(yy);
        end
        if yR > length(yy)
```

```
                yR = 1;
            end
            f(j) = f(j) + 1;
            rval = rand();
            if Z(xL,y) == z||Z(xR,y) == z||Z(x,yL) == z||
            Z(x,yR) == z||Z(x,y) == zD||Z(x,y) == zU
                if Pstick > rval
                    Z(x,y) = Z(x,y) + 1;
                    if Z(x,y) > Height
                        Height = Z(x,y);
                    end
                    break;
                end
            end
        end

        if i == nParticles || mod(i,nNewParticlesPerFrame) == 0
            surf(Z, 'EdgeColor', 'none');
            %colormap(1-prism);
            alpha(0.55);
            %axis equal
            %axis tight
            axis([0 maxX 0 maxY 0 20])
            drawnow
            shading interp
            grid on
        end
    end
end

title('P_{stick} = 0.99','FontSize',12);
```

```
fprintf('Height = %d\n',Height);

% End timing
toc
```

Stochastic simulation code on diffusion-dissolution-deposition code.

```
rng('default');
% Parameter initialization
L = 1;
K = 50;
h = L/K;
D = 1e-5;
kdif = D/h/h; % Diffusion rate (A -> A)
kdep = 1.2e-3; % Deposition rate (A -> phi)
kdis = 1.5e-3; % Dissolution rate (phi -> A)
%%%%%%%%%%%%%%%%%%%%%%%%%%%%%%%%%%%%%%%%%%%%%%%%%%%%%%%%
% Deposition happening with sticking coefficient nu
% Dissolution happening everywhere
%%%%%%%%%%%%%%%%%%%%%%%%%%%%%%%%%%%%%%%%%%%%%%%%%%%%%%%%
% Assume 5 areas with different overpotential
% High overpotential --> High sticking probability
nu = [0.1 0.3 0.5 0.7 0.9];
kdep = kdep * nu;

T = 30*60;
A0 = 100; % Initial number of ions on the surface
A = zeros(K,1);
A(:) = A0;
t = 0;
%%%%%%%%%%%%%%%%%%%%%%%%%%%%%%%%%%%%%%%%%%%%%%%%%%%%%%%%
```

```
while(t <= T)
% Initialize the propensity function
aDif = A*kdif;
aLeft = sum(aDif(1:K-1)); % Left propensity
aRight = sum(aDif(2:K)); % Right propensity
aDis = kdis; % Dissolution propensity
aDep1 = A(1:K/5)*kdep(1); % Deposition propensity area 1
aDep2 = A(K/5+1:K*2/5)*kdep(2); % Deposition propensity area 2
aDep3 = A(K*2/5+1:K*3/5)*kdep(3); % Deposition propensity area 3
aDep4 = A(K*3/5+1:K*4/5)*kdep(4); % Deposition propensity area 4
aDep5 = A(K*4/5+1:K)*kdep(5); % Deposition propensity area 5
sumDep1 = sum(aDep1);
sumDep2 = sum(aDep2);
sumDep3 = sum(aDep3);
sumDep4 = sum(aDep4);
sumDep5 = sum(aDep5);
aDep = sumDep1 + sumDep2 + sumDep3 + sumDep4 + sumDep5;
a0 = aLeft + aRight + K*aDis + aDep;

% Get the random number
r = rand(2,1);

% Update time
tau = (1/a0) * log(1/r(1));
t = t + tau;

% Choose which event to happen
% Go for left diffusion
if ((r(2)>=0) && (r(2)<aLeft/a0))
  for i = 1 : K-1
        if ((r(2)>=sum(aDif(1:i-1))/a0) && (r(2)<sum(aDif(1:i))/a0))
```

```
          A(i) = A(i) - 1;
          A(i+1) = A(i+1) + 1;
          break;
        end
      end

% Go for right diffusion
elseif ((r(2)>=aLeft/a0) && (r(2)<(aLeft+aRight)/a0))
  for i = 2 : K
        if ((r(2)>=(aLeft+sum(aDif(2:i-1)))/a0) &&
        (r(2)<(aLeft+sum(aDif(2:i)))/a0))
          A(i) = A(i) - 1;
          A(i-1) = A(i-1) + 1;
          break;
        end
    end

% Go for Deposition
% Area 1
elseif ((r(2)>=(aLeft+aRight)/a0) && (r(2)<(aLeft+aRight+sumDep1)/a0))
      for i = 1 : K/5
        if ((r(2)>=(aLeft+aRight+sum(aDep1(1:i-1)))/a0) &&
        (r(2)<(aLeft+aRight+sum(aDep1(1:i)))/a0))
          A(i) = A(i) - 1;
          break;
        end
      end

% Area 2
elseif ((r(2)>=(aLeft+aRight+sumDep1)/a0) &&
    (r(2)<(aLeft+aRight+sumDep1+sumDep2)/a0))
```

```
      for i = 1 : K/5
        if ((r(2)>=(aLeft+aRight+sumDep1+sum(aDep2(1:i-1)))/a0) &&
        (r(2)<(aLeft+aRight+sumDep1+sum(aDep2(1:i)))/a0))
          A(i+K/5) = A(i+K/5) - 1;
          break;
        end
      end

% Area 3
elseif ((r(2)>=(aLeft+aRight+sumDep1+sumDep2)/a0) &&
    (r(2)<(aLeft+aRight+sumDep1+sumDep2+sumDep3)/a0))
      for i = 1 : K/5
        if ((r(2)>=(aLeft+aRight+sumDep1+sumDep2+sum(aDep3(1:i-1)))/a0) &&
        (r(2)<(aLeft+aRight+sumDep1+sumDep2+sum(aDep3(1:i)))/a0))
          A(i+2*K/5) = A(i+2*K/5) - 1;
          break;
        end
      end

% Area 4
elseif ((r(2)>=(aLeft+aRight+sumDep1+sumDep2+sumDep3)/a0) &&
    (r(2)<(aLeft+aRight+sumDep1+sumDep2+sumDep3+sumDep4)/a0))
      for i = 1 : K/5
        if ((r(2)>=(aLeft+aRight+sumDep1+sumDep2+sumDep3
        +sum(aDep4(1:i-1)))/a0) && (r(2)<(aLeft+aRight+sumDep1
        +sumDep2+sumDep3+sum(aDep4(1:i)))/a0))
          A(i+3*K/5) = A(i+3*K/5) - 1;
          break;
        end
      end
```

```
% Area 5
elseif ((r(2)>=(aLeft+aRight+sumDep1+sumDep2+sumDep3+sumDep4)/a0) &&
     (r(2)<(aLeft+aRight+aDep)/a0))
      for i = 1 : K/5
        if ((r(2)>=(aLeft+aRight+sumDep1+sumDep2+sumDep3+
        sumDep4+sum(aDep5(1:i-1)))/a0) && (r(2)<(aLeft+aRight+
        sumDep1+sumDep2+sumDep3+sumDep4+sum(aDep5(1:i)))/a0))
          A(i+4*K/5) = A(i+4*K/5) - 1;
          break;
        end
      end

% Go for Dissolution
else
      for i = 1 : K
        if ((r(2)>=(aLeft+aRight+aDep+(i-1)*aDis)/a0) &&
        (r(2)<(aLeft+aRight+aDep+i*aDis)/a0))
          A(i) = A(i) + 1;
          break;
        end
      end
    end
end
%%%%%%%%%%%%%%%%%%%%%%%%%%%%%%%%%%%%%%%%%%%%%%%%%%%%%%%%%%%%%%%%
% Plot the figure
%%%%%%%%%%%%%%%%%%%%%%%%%%%%%%%%%%%%%%%%%%%%%%%%%%%%%%%%%%%%%%%%
xxx = [h/2 : h : L-h/2];
figure
set(gca, 'FontSize', 15);
bar(xxx, A);
colormap([0.8 0.8 0.8])
```

```
box on
xlabel('x [mm]')
ylabel('Number of Zn^{2+} Ions')
axis([0 1 0 1.2*max(A)])
text(0.1, max(A), 'time = 30 min', 'FontSize', 15);
title('Diffusion-Dissolution-Deposition')
```

COMSOL Multiphysics Setting

LMO Setting

$LiMn_2O_4$ setting are based on the parameters obtained from COMSOL.

```
Ds_pos 1e-13[m^2/s] Solid phase Li-diffusivity Positive
rp_pos 8e-6[m] Particle radius Positive
T 298[K] Temperature
t_plus 0.363 Cationic transport number
Dl 7.5e-11[m^2/s] Salt diffusivity in Electrolyte
epss_pos 1-epsl_pos-0.259 Solid phase vol-fraction Positive
epsl_pos 0.444 Electrolyte phase vol-fraction Positive
Ks_pos 3.8[S/m] Solid phase conductivity Positive
cl_0 2000[mol/m^3] Initial electrolyte salt concentration
csmax_pos 22860[mol/m^3] Max solid phase concentration Positive
cs0_pos 3900[mol/m^3] Initial Positive State of Charge
k_pos 2e-11[m/s] Reaction rate coefficient Positive
aA_pos 0.5 Reaction rate coefficient Positive
aC_pos 0.5 Reaction rate coefficient Positive
i_disch i_1C Discharge current
t_disch_stop 3600[s] Discharge duration
t_ocp 60[s] Open Circuit interval
i_charge -i_1C Charge current
```

```
t_charge_stop 3600[s] Charge time
n_count 0 multiplicative factor for cycle number counts
n_cyc 100 Cycle number
D_Li_ion 0.9e-15[m^2/s] Duffusion coefficient for Li ions in the electrolyte
D_n 5.1e-15[m^2/s] Diffusion coefficient for n in the electrolyte
Eq_Zn -0.763[V] Equilibrium potential for Zinc
disch_on step1((t-n_count*(t_disch_stop+t_charge_stop+2*t_ocp))[1/s])*
  step1((n_count*(t_disch_stop+t_charge_stop+2*t_ocp)+t_disch_stop-t)[1/s])
  discharge on/off func
charge_on step1((t-n_count*(t_disch_stop+t_charge_stop+2*t_ocp)-
  t_disch_stop-t_ocp)[1/s])*step1((n_count*(t_disch_stop+t_charge_stop+2*t_ocp)+
  t_charge_stop+t_disch_stop+t_ocp-t)[1/s]) charge on/off func
i_app i_disch*disch_on+i_charge*charge_on total charge/discharge current
```

Zn Corrosion Setting

Some of Zn corrosion study parameters.

```
DSO4 1e-9[m^2/s]
DLi 1e-9[m^2/s]
DZn2 1e-9[m^2/s]
DZnOH2 1e-9[m^2/s]
DH 9.3e-9[m^2/s]
DOH 5.3e-9[m^2/s]
DH2 1e-9[m^2/s]
DO2 1e-9[m^2/s]
DZnSO4 1e-9[m^2/s]
R 8.314[J/(mol*K)]
T 298[K]
F 96485.3415[C/mol]
a1 1
i01 2.7e11[A/m^2]
```

```
a2 0.5
i02 2e-7[A*m/mol]
kZnf 1e-3[m^3/mol]
kZnb (1e9)[m^3/mol]
Keauf 1e-3
keaub 1e8[m^6/mol^2]
c0_SO4 2000[mol/m^3]
c0_Zn2 1e-6[mol/m^3]
c0_ZnOH2 cWater^2*c0_Zn2*kZnf/(kZnb*c0_H^2)
c0_H 1e-4[mol/m^3]
c0_OH 1e-14[mol^2/m^6]/(c0_H)
c0_H2 0[mol/m^3]
c0_ZnSO4 1e-6[mol/m^3]
Vm -0.763[V]
cWater 1000[mol/m^3]
Kwater 1e-8[mol^2/m^6]
KZn 1e-12 Equilibrium Constant Zn2 + 2H2O = Zn(OH)2 + 2H
kSO4f 1[m^3/s/mol]
kSO4b 1e4[mol/m^3]
KZn1 1e13
KZn2 1e20
kZnOH2_1f 1e4[m^3/mol]
kZnOH2_1b 1e-6[m^3/mol]
kZnOH2_2f 1e6[m^3/mol]
kZnOH2_2b 1e-10[m^3/mol]
```

References

[1] R. Zito, *Energy Storage: A New Approach*. Scrivener Publishing LLC, 2010.

[2] W. Li, J. R. Dahn, and D. S. Wainwright, "Rechargeable lithium batteries with aqueous electrolytes," *Science*, vol. 264, pp. 1115–1118, 1994.

[3] G. Wang, L. Fu, N. Zhao, L. Yang, and Y. Wu, "An aqueous rechargeable lithium battery with good cycling performance," *Angewandte Chemie International Edition*, vol. 46, pp. 295–297, 2006.

[4] G. Wang, S. Zhong, D. Bradhurst, S. Dou, and H. Liu, "Secondary aqueous lithium-ion batteries with spinel anodes and cathodes," *Journal of Power Sources*, vol. 74, pp. 198–201, 1998.

[5] G. Wang, N. Zhao, L. Yang, Y. Wu, H. Wu, and R. Holze, "Characteristics of an aqueous rechargeable lithium battery (arlb)," *Electrochimica Acta*, vol. 52, no. 15, pp. 4911–4915, 2007.

[6] G. James *Science*, vol. 264, p. 1084, 1994.

[7] J. Yan, J. Wang, H. Liu, Z. Bakenov, D. Gosselink, and P. Chen, "Rechargeable hybrid aqueous batteries," *Journal of Power Sources*, vol. 216, pp. 222–226, 2012.

[8] E. Hosono, T. Kudo, I. Honma, H. Matsuda, and H. Zhou, "Synthesis of single crystalline spinel $LiMn_2O_4$ nanowires for a lithium ion battery with high power density," *Nano Lett.*, vol. 9, no. 3, pp. 1045–1051, 2008.

[9] A. R. Armstrong and P. G. Bruce, "Synthesis of layered $LiMn_2O_4$ as an electrode for rechargeable lithium batteries," *Nature*, vol. 381, pp. 499–500, 1996.

[10] R. Koksbang, J. Barker, H. Shi, and M. Saidi, "Cathode materials for lithium rocking chair batteries," *Solid State Ionics*, vol. 84, no. 1-2, pp. 1–21, 1995.

[11] M. S. Hong, S. H. Lee, and S. W. Kim, "Use of kcl aqueous electrolyte for 2v manganese oxide/activated carbon hybrid capacitor," *Electrochemical and Solid-State Letters*, vol. 5, no. 10, pp. A227–A230, 2002.

[12] Y. Yuan, H. Wu, S. Guo, J. Wu, J. Yang, X. Wang, and J. Tu, "Preparation, characteristics and electrochemical properties of surface-modified $LiMn_2O_4$ by doped $LiNi_{0.05}Mn_{1.95}O_4$,"

[13] B. G. E.P and D. N. R., *Empirical model-building and response surfaces*. Oxford, England John Wiley & Sons, 1987.

[14] H. Chan and D. Sutanto, "A new battery model for use with battery energy storage systems and electric vehicles power systems," *Institute of Electrical and Electronics Engineers*, vol. 1, pp. 470–475, 2000.

[15] G. T. Mase and G. E. Mase, *Continuum mechanics for engineers*. CRC Press LLC, 1999.

[16] N. P. Stevens and A. C. Fisher, "Finite element simulations in electrochemistry," *J. Phys. Chem. B*, vol. 101, pp. 8259–8263, 1997.

[17] G. Ning, R. E. White, and B. N. Popov, "A generalized cycle life model of rechargeable li-ion batteries," *Elecrochimica Acta*, vol. 51, pp. 2012–2022, 2005.

[18] "The comsol multiphysics reference guide," 2012.

[19] "The comsol multiphysics user's guide," 2012.

[20] J. Meller, "Molecular dynamics," *Encyclopedia of Life Science*, 2001.

[21] J. Hammersley and D. C. Handscomb, *Monte Carlo Methods*. Springer Netherlands, 1964.

[22] R. Y. Rubinstein and D. P. Kroese, *Simulation and Monte Carlo Method*. John Wiley & Sons, 2008.

[23] C. C. Battaile, "The kinetic monte carlo method: Foundation, implementation, and application," *Comput. Methods Appl. Mech. Engrg*, vol. 197, pp. 3386–3398, 2008.

[24] W. He, W. N., O. M., and P. M, "Remaining useful performance analysis of batteries," *Prognostics and Health Management (PHM), Institute of Electrical and Electronics Engineers*, pp. 1–6, 2011.

[25] R. Spotnitz, "Simulation of capacity fade in lithium-ion batteries," *Journal of Power Sources*, vol. 113, no. 1, pp. 72–80, 2003.

[26] B. Saha, G. K., P. S., and C. J., "An integrated approach to battery health monitoring using bayesian regression and state estimation," *Institute of Electrical and Electronics Engineers*, pp. 646–653, 2007.

[27] S. B. and G. K., "Uncertainty management for diagnostics and prognostics of batteries using bayesian techniques," 2008.

[28] I. Fernandez, C. Calvillo, A. Sanchez-Miralles, and J. Boal, "Capacity fade and aging models for electric batteries and optimal charging strategy for electric vehicles," *Energy*, vol. 60, pp. 35–43, 2013.

[29] W. Waag, C. Fleischer, and D. U. Sauer, "On-line estimation of lithium-ion battery impedance parameters using a novel varied-parameters approach," *Journal of Power Sources*, vol. 237, pp. 260–269, 2013.

[30] A. Miranda and C. Hong, "Integrated modeling for the cyclic behavior of high power li-ion batteries under extended operating conditions," *Applied Energy*, vol. 111, pp. 681–689, 2013.

[31] W. Gu, Z. Sun, X. Wei, and H. Dai, "A capacity fading model of lithium-ion battery cycle life based on the kinetics of side reactions for electric vehicle applications," *Electrochimica Acta*, vol. 133, pp. 107–116, 2014.

[32] P. Singh, R. Vinjamuri, X. Wang, and D. Reisner, "Fuzzy logic modeling of eis measurement on lithium-ion batteries," *Electrochimica Acta*, vol. 51, pp. 1673–1679, 2006.

[33] L. Kang, X. Zhao, and J. Ma, "A new neural network model for the state-of-charge estimation in the battery degradation process," *Applied Energy*, vol. 121, pp. 20–27, 2014.

[34] X. Chen, W. Shen, Z. Cao, and A. Kapoor, "Adaptive gain sliding mode observer for state of charge estimation based on combined battery equivalent circuit model," *Computers and Chemical Engineering*, vol. 64, pp. 114–123, 2014.

[35] E. P. Wigner, "The unreasonable effectiveness of mathematics in the natural sciences.," *Communications on Pure and Applied Mathematics*, vol. 13, no. 1, pp. 1–14, 1960.

[36] M. Doyle and J. Newman, "Comparison of modeling prediction with experimental data from plastic lithium ion cells," *Journal of Electrochemical Society*, vol. 143, 1996.

[37] P. Ramadass, B. Haran, Parthasarathy, M. Gomadam, R. White, and B. N. Popov, "Development of first principle capacity fade model for *Li-ion* cells," *Journal of Electrochemical Society*, vol. 151, no. 2, pp. A196–A203, 2004.

[38] G. Ning, R. E. White, and B. N. Popov, "A generalized cycle life model of rechargeable *Li-ion* batteries," *Electrochimica Acta*, vol. 51, no. 10, pp. 2012–2022, 2006.

[39] S. Sharland, C. Jackson, and A. Diver, "A finite-element model of the propagation of corrosion crevices and pits," *Corrosion Science*, vol. 29, no. 9, pp. 1149–1166, 1989.

[40] J. C. Walton, "Mathematical modeling of mass transport and chemical reaction in crevice and pitting corrosion," *Corrosion Science*, vol. 30, no. 8-9, pp. 915–928, 1990.

[41] S. Golmon, K. Maute, and M. L. Dunn, "A design optimization methodology for li^+ batteries," *Journal of Power Sources*, vol. 253, pp. 239–250, 2014.

[42] A. A. Pesaran, "Battery thermal models for hybrid vehicle simulation," *Journal of Power Sources*, vol. 110, pp. 377–382, 2002.

[43] R. Ball, R. Evans, and R. Stevens, "Finite element (FE) modeling of current density on the value regulated lead/acid battery positive grid," *Journal of Power Sources*, vol. 103, pp. 213–222, 2002.

[44] W.-J. Lai, M. Y. Ali, and J. Pan, "Mechanical behavior of representative volume elements of lithium-ion battery modules under various loading conditions," *Journal of Power Sources*, vol. 248, pp. 789–808, 2014.

[45] R. C. Alkire and R. D. Braatz, "Eletrochemical engineering in an age of discovery and innovation," *AlChE Journal*, vol. 50, no. 9, pp. 2000–2007, 2004.

[46] T. P. Merchant, M. K. Gobbert, T. S. Cale, and L. J. Borucki, "Multiple scale integrated modeling of deposition processes," *Thin Solid Films*, vol. 365, no. 2, pp. 368–375, 2000.

[47] W. N. Gill, D. J. Duquette, and D. Varadarajan, "Mass transfer models for the electrodeposition of copper with a buffer agent," *Journal of The Electrochemical Society*, vol. 148, no. 4, pp. C287–C296, 2001.

[48] A. Bortz, "A new algorithm for monte carlo simulation of ising spin systems," *Journal of Computational Physics*, vol. 17, no. 1, pp. 10–18, 1975.

[49] A. F. Voter, *Introduction to the Kinetic Monte Carlo Method*. Springer Netherlands, 2007.

[50] E. S. Hood, B. H. Toby, and W. H. Weinberg, "Precursor-mediated molecular chemisorption and thermal desorption: The interrelationships among energetics, kinetics and adsorbate lattice structure," *Physical Review Letter*, vol. 55, no. 22, pp. 2437–2240, 1985.

[51] P. A. Rikvold, "Simulations of a stochastic model for cluster growth on a square lattice," *Physical Review A*, vol. 26, no. 1, pp. 647–650, 1982.

[52] A. F. Voter, "Classically exact overlayer dynamics: Diffusion of rhodium clusters on rh(100)," *Physical Review B*, vol. 34, no. 10, pp. 6819–6829, 1986.

[53] T. O. Drews, R. D. Braatz, and R. C. Alkire, "Coarse-grained kinetic monte carlo simulation of copper electrodeposition with additives," *International Journal for Multiscale Computational Engineering*, vol. 2, no. 2, 2004.

[54] M. A. Katsoulakis and D. G. Vlachos, "Coarse-grained stochastic processes and kinetic monte carlo simulators for the diffusion of interacting particles," *The Journal of Chemical Physics*, vol. 119, p. 9412, 2003.

[55] M. A. Katsoulakis, A. J. Majda, and D. G. Vlachos, "Coarse-grained stochastic processes and monte carlo simulations in lattice systems," *Journal of Computational Physics*, vol. 186, no. 1, pp. 250–278, 2003.

[56] T. Treeratanaphitak, M. D. Pritzker, and N. M. Abukhdeir, "Kinetic monte carlo simulation of electrodeposition using the embedded-atom method," *Electrochimica Acta*, vol. 121, pp. 407–414, 2014.

[57] Z. Zheng, R. M. Stephens, R. D. Braatz, R. C. Alkire, and L. R. Petzold, "A hybrid multiscale kinetic monte carlo method for simulation of copper electrodeposition," *Journal of Computational Physics*, vol. 227, pp. 5184–5199, 2008.

[58] S. S. Ng, Y. Xing, and K. L. Tsui, "A naive bayes model for robust remaining useful life prediction of lithium-ion battery," *Applied Energy*, vol. 118, pp. 114–123, 2014.

[59] B. Pattipati, C. Sankavaram, and K. Pattipati, "System identification and estimation framework for pivotal automotive battery management system characteristics," *Systems Man, And Cybernetics IEEE*, vol. 41, no. 6, 2011.

[60] Y. He, X. Liu, C. Zhang, and Z. Chen, "A new model for state-of-charge (soc) estimation for high-power li-ion battery," *Applied Energy*, vol. 101, pp. 808–814, 2013.

[61] R. Xiong, F. Sun, X. Gong, and C. Gao, "A data-driven based adaptive state of charge estimator of lithium-ion polymer battery used in electric vehicles," *Applied Energy*, vol. 113, pp. 1421–1433, 2014.

[62] K. Goebel, B. Saha, A. Saxena, J. R. Celaya, and J. P. Christophersen, "Prognostics in battery health management," *IEEE Instrumentation & Measurement Magazine*, vol. 11, no. 4, p. 33, 2008.

[63] A. J. Smith, J. C. Burns, and J. R. Dahn, "A high precision study of the columbic efficiency of li-ion batteries," *Electrochemical and Solid-State Letters*, vol. 13, pp. A177–A179, 2010.

[64] M. S. Arulampalam, S. Maskell, N. Gordon, and T. Clapp, "A tutorial on particle filters for online nonlinear/non-gaussian bayesian tracking," *Institute of Electrical and Electronics Engineers*, vol. 50, no. 2, 2002.

[65] A. J. Smith, J. C. Burns, S. Trussler, and J. R. Dahn, "Precision measurements of the coulombic efficiency of lithium-ion batteries and of electrode materials for lithium-ion batteries," *Journal of The Electrochemical Society*, vol. 157, no. 2, pp. A196–A202, 2010.

[66] A. J. Smith, J. C. Burns, X. Zhao, D. Xiong, and J. R. Dahn, "A high precision coulometry study of the sei growth in li/graphite cells," *Journal of The Electrochemical Society*, vol. 158, no. 5, pp. A447–A452, 2011.

[67] T. M. Bond, J. C. Burns, D. A. Stevens, H. M. Dahn, and J. R. Dahn, "Improving precision and accuracy in coulombic efficiency measurements of li-ion batteries," *Journal of The Electrochemical Society*, vol. 160, no. 3, pp. A521–A527, 2013.

[68] A. J. Smith, J. C. Burns, D. Xiong, and J. R. Dahn, "Interpreting high precision coulometry results on li-ion cells," *Journal of The Electrochemical Society*, vol. 158, no. 10, pp. A1136–A1142, 2011.

[69] J. C. Burns, G. Jain, A. J. Smith, K. W. Eberman, E. Scott, J. P. Gardner, and J. R. Dahn, "Evaluation of effects of additives in wound li-ion cells through high precision

coulometry," *Journal of The Electrochemical Society*, vol. 158, no. 3, pp. A255–A261, 2011.

[70] "Hsc chemistry 5 chemical reaction and equilibrium software with extensive thermochemical database." Included in the software.

[71] X. G. Zhang, *Corrosion and Electrochemistry of Zinc*. Springer, 1996.

[72] E. Budevski, G. Staikov, and W. J. Lorenz, *Electrochemical Phase Formation and Growth: An Introduction to the Initial Stages of Metal Deposition*. 1996.

[73] L. Guo and P. C.Searson, "On the influence of the nucleation overpotential on island growth in electrodeposition," *Electrochimica Acta*, vol. 55, pp. 4086–4091, 2010.

[74] S. C. Hill and J. I. D. Alexander, "Modified diffusion-limited aggregation simulation of electrodeposition in two dimensions," *Physical Review E*, vol. 56, no. 4, 1997.

[75] R. Ravi, A. S. Raj, T. Parthiban, G. Radhakrishnan, and R. Kalidoss, "Computer simulation studies on electrodeposition of zinc," *Materials Chemistry and Physics*, vol. 34, pp. 290–294, 1993.

[76] R. F. Voss and M. Tomkiewicz, "Computer simulation of dendrite electrodeposition," *Journal of Electrochemical Society*, vol. 132, no. 2, 1985.

[77] D. T. Gillespie, "Exact stochastic simulation of coupled chemical reactions," *Journal of Physical Chemistry*, vol. 81, pp. 2340–2361, 1977.

[78] A. C. Levi and M. Kotrla, "Theory and simulation of crystal growth," *Journal of Physics Condensed Matter*, vol. 9, pp. 299–344, 1997.

[79] S. S. Andrews and D. Bray, "Stochastic simulation of chemical reactions with spatial resolution and single molecule detail," *Physical Biology*, vol. 1, pp. 137–151, 2004.

[80] L. Arnold, *Stochastic Differential Equations, theory and applications*. 1974.

[81] C. Clark, "Simulation and development of nanoscale deposition techniques using kinetic monte carlo," *PhD Thesis The University of Texas at Arlington*, 2007.